

Smart element method II. An element based on the finite Eshelby tensor

Gang Wang, Xiaohu Liu, Shaofan Li^{*,†} and Nicholas Sitar

Department of Civil and Environmental Engineering, University of California, Berkeley, CA 94720, U.S.A.

SUMMARY

In this study, we apply the newly derived finite Eshelby tensor in a variational multiscale formulation to construct a smart element through a more accurate homogenization procedure. The so-called Neumann–Eshelby tensor for an inclusion in a finite domain is used in the fine scale feedback procedure to take into account the interactions among different scales and elements.

Numerical experiments have been conducted to compare the performance and robustness of the new element to earlier formulations. The results showed that the smart element constructed via the Neumann–Eshelby tensor of a finite domain provides better numerical accuracy than that constructed via the Eshelby tensor of an infinite domain. Moreover, it can relieve volumetric locking. Copyright © 2005 John Wiley & Sons, Ltd.

KEY WORDS: eigenstrain method; Eshelby tensors; feedback finite element; homogenization; variational multiscale method

1. INTRODUCTION

In Part I of this work [1], the authors constructed a so-called smart element based on the variational eigenstrain multiscale method. The essential part of the smart element method is its built-in numerical error feedback control algorithm, which enables the element to self-adjust and self-adapt discretization errors, and hence achieve better computational accuracy in a coarse scale computation by homogenizing the discretization error of a given mesh.

In Part I, a smart element is constructed for linear elasticity problems via Zienkiewicz–Zhu posteriori estimate, which can automatically sense its own discretization error and adjust it. A main feature of the smart element method is that it provides a systematic and analytical procedure to construct the element Green’s function, or the related element Eshelby tensor, in the variational multiscale method. Previously this could only be achieved numerically.

*Correspondence to: Shaofan Li, Department of Civil and Environmental Engineering, University of California, Berkeley, CA 94720, U.S.A.

†E-mail: li@ce.berkeley.edu

Contract/grant sponsor: NSF; contract/grant numbers: CMS-0239130, EEC-9701568

Received 20 February 2005

Revised 18 May 2005

Accepted 23 May 2005

However, the above proposed element has some limitations, one of which is that it assumes the contribution of the disturbance field on the elemental boundary is small and negligible. This assumption simplifies the formulation and allows the use of the Eshelby tensor of the infinite space in the multiscale formulation. However, the approximation is only appropriate if the size of an inclusion, or the size of an element, is infinitesimal relative to the size of the total domain. It may be a bad approximation for a coarse mesh discretization, and it could undermine the performance of the proposed method. The current study aims to reformulate variational multiscale eigenstrain formulation without relying on such an approximation, rendering a more accurate smart element method.

Such a refined multiscale formulation is made possible by exploiting the so-called finite Eshelby tensors, recently derived by the authors [2, 3]. While the infinite Eshelby tensor fails to take into account of the prescribed boundary conditions, the finite Eshelby tensor incorporates these conditions.

The organization of the paper is as follows: Section 2 outlines the inclusion solution in a finite domain and the recently derived Neumann–Eshelby tensor. In Section 3, we reformulate the variational eigenstrain multiscale scheme by utilizing the finite Eshelby tensor to find the fine scale solution. Detailed algorithm for the finite element implementation is also provided. In Section 4, we discuss the performance of the proposed element in its ability to avoid volumetric locking through modal analysis. A few numerical examples are demonstrated in Section 5, followed by the conclusions in Section 6.

2. FINITE ESHELBY TENSOR FOR A CIRCULAR DOMAIN

As mentioned above, the essence of the so-called variational multiscale eigenstrain method [1, 4] is to utilize micromechanics technique (e.g. Reference [5]) to construct the element Eshelby tensor that links the coarse scale residual to the fine scale strain. This step is usually accomplished by utilizing the so-called element Green's function, which, in most cases, can only be obtained numerically.

The finite Eshelby tensor can be approximately used as the element Eshelby tensor. The detailed procedures on how to find the finite Eshelby tensor for a circular inclusion in a circular RVE under prescribed Dirichlet and Neumann boundaries have been reported in References [2, 3], respectively.

Consider a circular inclusion, Ω_e , embedded at the centre of a circular representative volume element (RVE), Ω_e^c , as shown in Figure 1. As a source of inhomogeneity, stiffness contrast between the inclusion and the matrix will cause a disturbance field inside the RVE. For prescribed traction (Neumann) boundary, the following holds for the disturbance stress field σ'_{ij} on the boundary of the RVE:

$$\sigma'_{ij}(\mathbf{x})n_j(\mathbf{x}) = 0 \quad \forall \mathbf{x} \in \partial\Omega_e^c \quad (1)$$

where σ'_{ij} is the disturbance stress field.

To account for the misfit of an inclusion, a piecewise constant eigenstrain field is introduced inside the RVE such that the disturbance stress and strain fields are related as

$$\sigma'_{ij}(\mathbf{x}) = \mathbb{C}_{ijkl}(\varepsilon'_{ij}(\mathbf{x}) - \varepsilon_{ij}^*(\mathbf{x})) \quad \forall \mathbf{x} \in \Omega_e^c \quad (2)$$

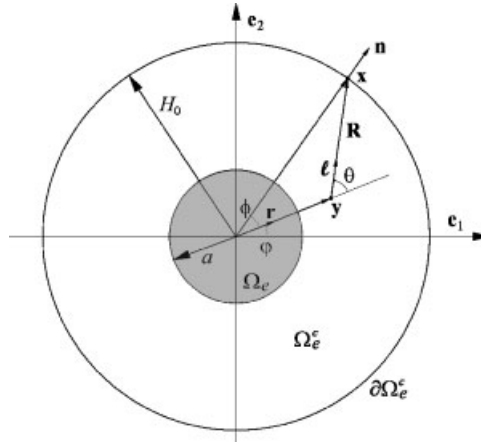


Figure 1. A circular representative element containing a circular inclusion.

where \mathbb{C}_{ijkl} is the elasticity tensor, and

$$\varepsilon_{ij}^*(\mathbf{x}) = \begin{cases} \varepsilon_{ij}^* & \forall \mathbf{x} \in \Omega_e \\ 0 & \forall \mathbf{x} \in \Omega_e^c / \Omega_e \end{cases} \quad (3)$$

The equilibrium equation, $\sigma'_{ji,j}(\mathbf{x}) = 0$, leads to the following boundary value problem:

$$\mathbb{C}_{ijkl} u'_{k, \ell j}(\mathbf{x}) - \mathbb{C}_{ijkl} \varepsilon_{kl}^*(\mathbf{x}) = 0 \quad \forall \mathbf{x} \in \Omega_e^c \quad (4)$$

$$\sigma'_{ij}(\mathbf{x}) n_j(\mathbf{x}) = 0 \quad \forall \mathbf{x} \in \partial \Omega_e^c \quad (5)$$

It is noted that the eigenstrain distribution is localized within the inclusion, and it is not present on the RVE boundary.

Using Somigliana's identity [6] and considering the prescribed traction boundary condition, the disturbance displacement field may be written as a Fredholm type integral equation for the disturbance displacement field \mathbf{u}' , i.e.

$$u'_i(\mathbf{y}) = \oint_{\partial \Omega_e^c} \mathbb{C}_{mnkl} u'_k(\mathbf{x}) G_{im,n}^\infty(\mathbf{y} - \mathbf{x}) n_\ell(\mathbf{x}) dS_x - \int_{\Omega_e} \mathbb{C}_{mnkl} G_{im,n}^\infty(\mathbf{y} - \mathbf{x}) \varepsilon_{kl}^*(\mathbf{x}) d\Omega_x \quad (6)$$

where $G_{mk}^\infty(\mathbf{y} - \mathbf{x})$ is so-called Green's function solving the following Navier's equation for an infinite elastic domain in a two-dimensional space,

$$\mathbb{C}_{ijkl} G_{mk, \ell j}^\infty(\mathbf{y} - \mathbf{x}) + \delta_{mi} \delta(\mathbf{y} - \mathbf{x}) = 0 \quad \forall \mathbf{x}, \mathbf{y} \in \mathbb{R}^2 \quad (7)$$

and

$$G_{ij}^\infty(\mathbf{y} - \mathbf{x}) = \frac{1}{8\pi\mu(1-\nu)} \left\{ \frac{(y_i - x_i)(y_j - x_j)}{|\mathbf{y} - \mathbf{x}|^2} - (3 - 4\nu)\delta_{ij} \ln |\mathbf{y} - \mathbf{x}| \right\} \quad (8)$$

where ν is Poisson's ratio, μ is shear modulus.

For an RVE of infinite size, boundary integration term in Equation (6) vanishes. Taking derivative of the remaining domain integral leads to the well-known infinite space Eshelby tensor $\mathbb{S}_{ijmn}^{I,\infty}$ [7–9], which is a constant inside an elliptical inclusion

$$\varepsilon'_{ij}(\mathbf{y}) = u'_{(i,j)}(\mathbf{y}) = \mathbb{S}_{ijmn}^{I,\infty} \varepsilon_{mn}^* \quad \forall \mathbf{y} \in \Omega_e \tag{9}$$

In general, the size of an RVE cannot be assumed infinite. Equation (6) needs to be evaluated exactly to take into account the influence of boundary condition prescribed if the RVE is finite. We aim to find the interior/exterior Neumann–Eshelby tensors ($\mathbb{S}_{ijmn}^{I,F}, \mathbb{S}_{ijmn}^{E,F}$) for a finite domain, analogous to the Eshelby tensor for an infinite space, to characterize the disturbance strain field in terms of the prescribed eigenstrain for a finite RVE under the Neumann boundary condition, such that,

$$\varepsilon'_{ij}(\mathbf{y}) = u'_{(i,j)}(\mathbf{y}) = \begin{cases} \mathbb{S}_{ijmn}^{I,F}(\mathbf{y}) \varepsilon_{mn}^* & \forall \mathbf{y} \in \Omega_e \\ \mathbb{S}_{ijmn}^{E,F}(\mathbf{y}) \varepsilon_{mn}^* & \forall \mathbf{y} \in \Omega_e^c/\Omega_e \end{cases} \tag{10}$$

For a circular inclusion embedded in a circular RVE under prescribed traction boundary condition, Equation (6) can be solved analytically on the strength of symmetry and radial isotropy. As derived in Reference [3], and also briefly outlined in Appendix A, the closed-form expressions for the Neumann–Eshelby tensors for interior and exterior points are given as follows:

$$\begin{aligned} \mathbb{S}_{ijmn}^{I,F}(\mathbf{y}) = & \frac{1}{8(1-v)} \{ [(4v-1)(1-\rho_0^2) - 3\rho_0^2(1-\rho_0^2)(1-4vt^2)] \delta_{ij} \delta_{mn} \\ & + [(3-4v) + \rho_0^2 + 3\rho_0^2(1-\rho_0^2)(1-2t^2)] (\delta_{im} \delta_{jn} + \delta_{in} \delta_{jm}) \\ & + [12(1-2v)\rho_0^2(1-\rho_0^2)t^2] \delta_{ij} r_m r_n \} \quad \forall \mathbf{y} \in \Omega_e \end{aligned} \tag{11}$$

$$\begin{aligned} \mathbb{S}_{ijmn}^{E,F}(\mathbf{y}) = & \frac{\rho_0^2}{8(1-v)} \left\{ \left[-2(1+2v) \left(\frac{1}{t^2} + 1 \right) + 12vt^2 + \rho_0^2 \left(\frac{9}{t^4} + 3 - 12vt^2 \right) \right] \delta_{ij} \delta_{mn} \right. \\ & + \left[\frac{2}{t^2} + 4 - 6t^2 - 3\rho_0^2 \left(\frac{1}{t^4} + 1 - 2t^2 \right) \right] (\delta_{im} \delta_{jn} + \delta_{in} \delta_{jm}) \\ & + \left[4 \left(\frac{1+2v}{t^2} + 3(1-2v)t^2 \right) - 12\rho_0^2 \left(\frac{1}{t^4} + (1-2v)t^2 \right) \right] \delta_{ij} r_m r_n \\ & \left. + \left[\frac{4}{t^2} \left(1 - \frac{3\rho_0^2}{t^2} \right) \right] \delta_{mn} r_i r_j + \left[\frac{8}{t^2} \left(\frac{3\rho_0^2}{t^2} - 2 \right) \right] r_i r_j r_m r_n \right\} \quad \forall \mathbf{y} \in \Omega_e^c/\Omega_e \end{aligned} \tag{12}$$

where $r_i = y_i/|\mathbf{y}|$ is the unit normal vector, $t = |\mathbf{y}|/H_0$ is the normalized radial position, $\rho_0 = a/H_0$ is the ratio of the inclusion and RVE radius. The interior/exterior Neumann–Eshelby tensor is position dependent and ‘radially isotropic’, in contrast to the well-known infinite space Eshelby tensor which is constant and isotropic. As a mean of homogenization, we are prompted

to average the interior Neumann–Eshelby tensor over the circular inclusion, and the average is found being isotropic.

Using average operator $\langle \bullet \rangle_{\Omega_e} := (1/\pi a^2) \int_{\Omega_e} \bullet \, d\Omega$, it is easy to evaluate

$$\langle t^2 \rangle_{\Omega_e} = \frac{1}{2} \rho_0^2, \quad \langle t^2 n_m n_n \rangle_{\Omega_e} = \frac{1}{4} \rho_0^2 \delta_{mn} \tag{13}$$

and the volume fraction of the inclusion in an RVE is defined as

$$f := \rho_0^2 = \frac{a^2}{H_0^2} \tag{14}$$

The average interior Neumann–Eshelby tensor from Equation (11) has the following form:

$$\begin{aligned} \langle \mathbb{S}_{ijmn}^{I,F} \rangle_{\Omega_e} &= s_1^F \mathbb{E}_{ijmn}^{(1)} + s_2^F \mathbb{E}_{ijmn}^{(2)} \\ &= \frac{1 + (1 - 2\nu)f}{2(1 - \nu)} \mathbb{E}_{ijmn}^{(1)} + \frac{(3 - 4\nu) + f(4 - f(6 - 3f))}{4(1 - \nu)} \mathbb{E}_{ijmn}^{(2)} \end{aligned} \tag{15}$$

in which the tensorial bases $E_{ijmn}^{(1)}$ and $E_{ijmn}^{(2)}$ span an fourth-order isotropic tensor space, and they are defined as

$$\mathbb{E}_{ijmn}^{(1)} = \frac{1}{2} \delta_{ij} \delta_{mn} \tag{16}$$

$$\mathbb{E}_{ijmn}^{(2)} = \frac{1}{2} (\delta_{im} \delta_{jn} + \delta_{in} \delta_{jm} - \delta_{ij} \delta_{mn}) \tag{17}$$

One may compare this result with the interior Eshelby tensor of an infinite space, which is given as

$$\mathbb{S}_{ijmn}^{I,\infty} = s_1^\infty \mathbb{E}_{ijmn}^{(1)} + s_2^\infty \mathbb{E}_{ijmn}^{(2)} = \frac{1}{2(1 - \nu)} \mathbb{E}_{ijmn}^{(1)} + \frac{3 - 4\nu}{4(1 - \nu)} \mathbb{E}_{ijmn}^{(2)} \tag{18}$$

Incorporating the prescribed boundary conditions, the (average) Neumann–Eshelby tensor is enriched by taking into account of the volume fraction of the inclusion f , which serves as a scalar indicator for the magnitude of inhomogeneity. Compared to the original Eshelby tensor, the Neumann–Eshelby tensor greatly enhances the description of the disturbance fields. Note that for the limiting case of dilute distribution ($f = 0$), the Neumann–Eshelby tensor degenerates to the original Eshelby tensor (i.e. $s_1^F = s_1^\infty$, and $s_2^F = s_2^\infty$). While for $f = 1$, $s_1^F = 1$ and $s_2^F = 1$. Figure 2 plots against f the coefficients of Neumann–Eshelby tensor (s_1^F, s_2^F) and the original Eshelby tensor (s_1^∞, s_2^∞) for $\nu = 0.1$. As indicated in the figure, the coefficients for the Eshelby tensor in the unbounded space do not change as the volume fraction of the second phase increases, whereas the coefficients of the Neumann–Eshelby tensor change with the volume fraction of the second phase. At both ends (i.e. $f = 0$ and 1), the Neumann–Eshelby tensor provides the exact solution. This is because that the Neumann–Eshelby tensor takes into account both the boundary effect (image force effect) and the effect of the finite size of an RVE. Therefore,

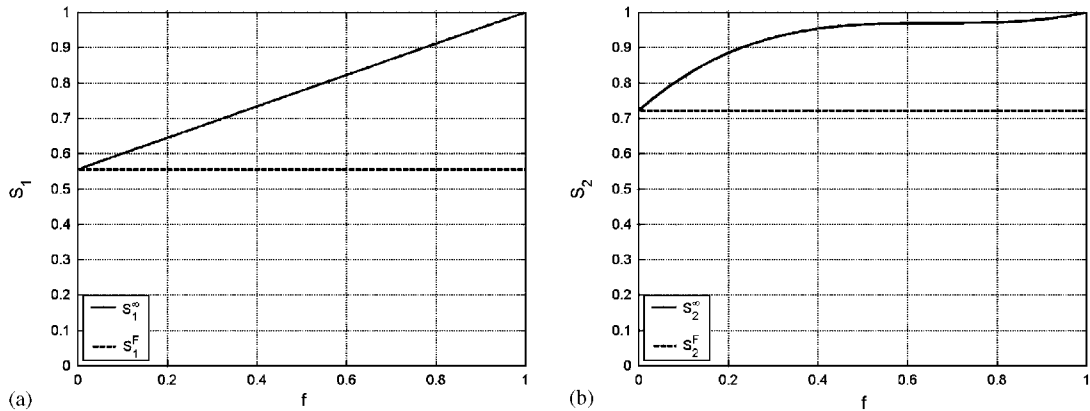


Figure 2. Comparison of S^F and S^∞ : (a) s_1^F vs s_1^∞ ; and (b) s_2^F vs s_2^∞ .

the accuracy of the prediction based on using the eigenstrain method in terms of the Eshelby tensor is greatly improved especially in the case of dense inclusion distribution.

3. VARIATIONAL MULTISCALE FORMULATION

3.1. Two-scale formulation

We now reformulate the variational eigenstrain multiscale formulation in the context of linear elasticity theory.

Consider a simply connected domain, $\Omega \in \mathbb{R}^d$ (d is the dimension of the physical space). Denote the body force b_i , prescribed displacement $u_i^0, \forall \mathbf{x} \in \Gamma_u$, and prescribed traction $t_i^0, \forall \mathbf{x} \in \Gamma_t$, where $\Gamma_u \cup \Gamma_t = \partial\Omega$ and $\Gamma_u \cap \Gamma_t = \emptyset$. The variational statement of the boundary value problem of elastostatics is,

Find $\mathbf{u} \in \mathcal{S}$ such that

$$\int_{\Omega} w_{(i,j)} \mathbb{C}_{ijkl} u_{(k,\ell)} \, d\Omega = \int_{\Omega} w_i b_i \, d\Omega + \int_{\Gamma_t} w_i t_i^0 \, dS \quad \forall \mathbf{w} = w_i \mathbf{e}_i \in \mathcal{V} \tag{19}$$

where \mathbb{C}_{ijkl} is the elastic tensor. The generalized Hooke's law $\sigma_{ij} = \mathbb{C}_{ijkl} \varepsilon_{kl}$ is implied for Cauchy stress σ_{ij} and infinitesimal strain $\varepsilon_{ij} = u_{(i,j)}$. Without elaboration, the trial function space \mathcal{S} and the test function space \mathcal{V} are defined here using standard notations in functional analysis (e.g. References [10, 11]),

$$\mathcal{S} = \{\mathbf{u}(\mathbf{x}) | \mathbf{u}(\mathbf{x}) \in [H^1(\Omega)]^d, \mathbf{u} = \mathbf{u}^0 \quad \forall \mathbf{x} \in \Gamma_u\} \tag{20}$$

$$\mathcal{V} = \{\mathbf{w}(\mathbf{x}) | \mathbf{w}(\mathbf{x}) \in [H^1(\Omega)]^d, \mathbf{w} = \mathbf{0} \quad \forall \mathbf{x} \in \Gamma_u\} \tag{21}$$

Define an abstract notation,

$$a(\mathbf{w}, \mathbf{u}) : \mathcal{V} \times \mathcal{S} \rightarrow \mathbb{R}, \quad a(\mathbf{w}, \mathbf{u}) := \int_{\Omega} (\nabla \otimes \mathbf{w}) : \mathbf{C} : (\nabla \otimes \mathbf{u}) \, d\Omega \tag{22}$$

and two linear forms

$$(\mathbf{w}, \mathbf{b})_{\Omega} : \mathcal{V} \times [H^{-1}(\Omega)]^d \rightarrow \mathbb{R}, \quad (\mathbf{w}, \mathbf{b})_{\Omega} := \int_{\Omega} \mathbf{w} \cdot \mathbf{b} \, d\Omega \tag{23}$$

$$(\mathbf{w}, \mathbf{t})_{\Gamma_t} : \mathcal{V} \times [H^{1/2}(\Omega)]^d \rightarrow \mathbb{R}, \quad (\mathbf{w}, \mathbf{t})_{\Gamma_t} := \int_{\Gamma_t} \mathbf{w} \cdot \mathbf{t} \, dS \tag{24}$$

The weak form (19) can be written in the compact form

$$a(\mathbf{w}, \mathbf{u}) = (\mathbf{w}, \mathbf{b})_{\Omega} + (\mathbf{w}, \mathbf{t}^0)_{\Gamma_t} \quad \forall \mathbf{w} \in \mathcal{V} \tag{25}$$

Following Hughes *et al.* [12], we assume that the exact solution of the weak form (25) can be decomposed into two solutions with different spatial resolutions, i.e.

$$\mathbf{u} = \bar{\mathbf{u}} + \mathbf{u}' \tag{26}$$

$$\mathbf{w} = \bar{\mathbf{w}} + \mathbf{w}' \tag{27}$$

where $\bar{\mathbf{u}}$ and \mathbf{u}' represent the coarse scale and fine scale solutions. $\bar{\mathbf{w}}$ and \mathbf{w}' represent coarse scale and fine scale trial functions, respectively. Accordingly, the trial function space and test function space can be additively decomposed into a coarse scale space and a fine scale space, i.e. $\mathcal{S} = \bar{\mathcal{S}} \oplus \mathcal{S}'$. $\mathcal{V} = \bar{\mathcal{V}} \oplus \mathcal{V}'$. Since coarse scale spaces are to be solved numerically, $\bar{\mathcal{S}}$ and $\bar{\mathcal{V}}$ are finite dimensional spaces. On the other hand, the fine scale is to be sought analytically so \mathcal{S}' and \mathcal{V}' belong to infinite-dimensional function spaces.

Under two-scale decomposition and consider \mathbf{w} and \mathbf{u} are independent, the weak form (25) then becomes

$$a(\bar{\mathbf{w}}, \bar{\mathbf{u}}) + a(\bar{\mathbf{w}}, \mathbf{u}') = (\bar{\mathbf{w}}, \mathbf{b})_{\Omega} + (\bar{\mathbf{w}}, \mathbf{t}^0)_{\Gamma_t} \quad \forall \bar{\mathbf{w}} \in \bar{\mathcal{V}} \tag{28}$$

$$a(\mathbf{w}', \bar{\mathbf{u}}) + a(\mathbf{w}', \mathbf{u}') = (\mathbf{w}', \mathbf{b})_{\Omega} + (\mathbf{w}', \mathbf{t}^0)_{\Gamma_t} \quad \forall \mathbf{w}' \in \mathcal{V}' \tag{29}$$

3.2. Fine scale solution

To obtain fine scale solution analytically, we examine the two scale relation at a typical local domain, $\Omega_e^c \subset \Omega \in \mathbb{R}^2$. The local domain is chosen as a circular shape (superscript ‘c’), and it is the smallest circle that encompasses the element e (subscript ‘e’), as illustrated in Figure 3. Within Ω_e^c ,

$$\mathbb{C}_{ijkl} u'_{k, \ell j}(\mathbf{x}) + \mathbb{C}_{ijkl} \bar{u}_{k, \ell j}(\mathbf{x}) + b_i(\mathbf{x}) = 0 \quad \forall \mathbf{x} \in \Omega_e^c \tag{30}$$

Note that this is not a boundary value problem, because around the boundary of the local domain, $\partial\Omega_e^c$, both displacement and traction are not prescribed.

To obtain the fine scale solution in the local domain, the above equilibrium equation is written in weak form,

$$\int_{\Omega_e^c} (\mathbb{C}_{mnkl} u'_{k, \ell n}(\mathbf{x}) + \mathbb{C}_{mnkl} \bar{u}_{k, \ell n}(\mathbf{x}) + b_m(\mathbf{x})) G_{im}^{\infty}(\mathbf{y} - \mathbf{x}) \, d\Omega_x = 0 \quad \forall \mathbf{x} \in \Omega_e^c \tag{31}$$

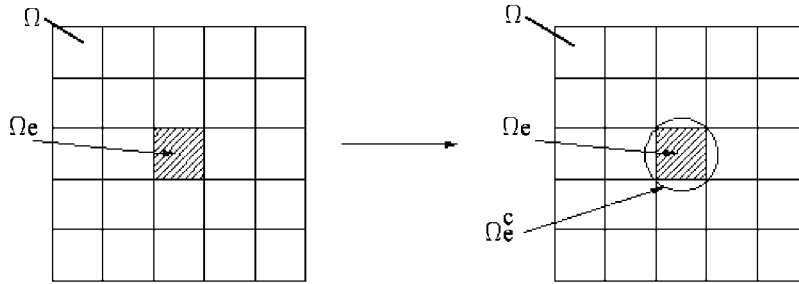


Figure 3. Illustration of the concept of equivalent element domain Ω_e^c .

which reduces to the Somigliana identity [6] to express the fine scale solution as the following integral form:

$$u'_i(\mathbf{y}) = \int_{\Omega_e^c} (\mathbb{C}_{mnk\ell} \bar{u}_{k,\ell n}(\mathbf{x}) + b_m(\mathbf{x})) G_{im}^\infty(\mathbf{y} - \mathbf{x}) \, d\Omega_x + \int_{\partial\Omega_e^c} \sigma'_{mn}(\mathbf{x}) n_n(\mathbf{x}) G_{im}^\infty(\mathbf{y} - \mathbf{x}) \, dS_x + \int_{\partial\Omega_e^c} \sigma_{k\ell}^{G_i^\infty}(\mathbf{y} - \mathbf{x}) n_\ell(\mathbf{x}) u'_k(\mathbf{x}) \, dS_x \quad (32)$$

where $u'_k(\mathbf{x})$ is the fine scale displacement, $\sigma'_{mn}(\mathbf{x}) = \mathbb{C}_{mnkl} u'_{k,\ell}(\mathbf{x})$ is the corresponding fine scale stress component, $G_{im}^\infty(\mathbf{y} - \mathbf{x})$ is Green's function of the Navier equation of linear elasticity in an infinite domain, $\sigma_{k\ell}^{G_i^\infty}(\mathbf{y} - \mathbf{x}) = \mathbb{C}_{mnk\ell} G_{im,n}^\infty(\mathbf{y} - \mathbf{x})$ is the stress of Green's function, and $n_\ell(\mathbf{x})$ is the out-normal of the surface $\partial\Omega_e^c$ at position \mathbf{x} . The subscript x in the term $d\Omega_x$ and dS_x of the above equation denotes that the integral is evaluated with respect to the variable \mathbf{x} . The derivative $G_{im,n}^\infty(\mathbf{y} - \mathbf{x}) = (\partial/\partial y_n) G_{im}^\infty(\mathbf{y} - \mathbf{x}) = -(\partial/\partial x_n) G_{im}^\infty(\mathbf{y} - \mathbf{x})$.

In Part I of this work, it is assumed that all the boundary contributions from the fine scale solution are small, and the following approximations are adopted:

$$\int_{\partial\Omega_e^c} \sigma'_{ij}(\mathbf{x}) n_j(\mathbf{x}) G_{im}^\infty(\mathbf{y} - \mathbf{x}) \, dS_x \approx 0 \quad (33)$$

$$\int_{\partial\Omega_e^c} \sigma_{k\ell}^{G_i^\infty}(\mathbf{y} - \mathbf{x}) n_\ell(\mathbf{x}) u'_k(\mathbf{x}) \, dS_x \approx 0 \quad (34)$$

In general, neglecting the boundary contribution can lead to considerable error in numerical computation. In this paper, we will proceed without such an approximation.

Integrating Equation (32) by parts yields

$$u'_i(\mathbf{y}) = \int_{\Omega_e^c} \mathbb{C}_{mnk\ell} \bar{u}_{k,\ell}(\mathbf{x}) G_{im,n}^\infty(\mathbf{y} - \mathbf{x}) \, d\Omega_x + \int_{\Omega_e^c} b_m(\mathbf{x}) G_{im}^\infty(\mathbf{y} - \mathbf{x}) \, d\Omega_x + \int_{\partial\Omega_e^c} \sigma_{mn}(\mathbf{x}) n_n(\mathbf{x}) G_{im}^\infty(\mathbf{y} - \mathbf{x}) \, dS_x + \int_{\partial\Omega_e^c} \sigma_{k\ell}^{G_i^\infty}(\mathbf{y} - \mathbf{x}) n_\ell(\mathbf{x}) u'_k(\mathbf{x}) \, dS_x \quad (35)$$

Note that by definition, $\sigma_{mn}(\mathbf{x}) = \bar{\sigma}_{mn}(\mathbf{x}) + \sigma'_{mn}(\mathbf{x})$.

Consider the weak form of the equilibrium equation, $\sigma_{mn,n}(\mathbf{x}) + b_m(\mathbf{x}) = 0, \forall \mathbf{x} \in \Omega_e^c$,

$$\int_{\Omega_e^c} (\sigma_{mn,n}(\mathbf{x}) + b_m(\mathbf{x})) G_{im}^\infty(\mathbf{y} - \mathbf{x}) d\Omega_x = 0 \tag{36}$$

Integrating Equation (36) by parts yields,

$$\int_{\partial\Omega_e^c} \sigma_{mn}(\mathbf{x}) n_n(\mathbf{x}) G_{im}^\infty(\mathbf{y} - \mathbf{x}) dS_x + \int_{\Omega_e^c} b_m(\mathbf{x}) G_{im}^\infty(\mathbf{y} - \mathbf{x}) d\Omega_x = - \int_{\Omega_e^c} \sigma_{mn}(\mathbf{x}) G_{im,n}^\infty(\mathbf{y} - \mathbf{x}) d\Omega_x \tag{37}$$

Substituting Equation (37) into Equation (35), we have

$$u'_i(\mathbf{y}) = \int_{\Omega_e^c} C_{mnkl} (\bar{u}_{k,\ell}(\mathbf{x}) - u_{k,\ell}(\mathbf{x})) G_{im,n}^\infty(\mathbf{y} - \mathbf{x}) d\Omega_x + \int_{\partial\Omega_e^c} \sigma_{kl}^{G_i^\infty}(\mathbf{y} - \mathbf{x}) n_\ell(\mathbf{x}) u'_k(\mathbf{x}) dS_x \tag{38}$$

Involving various approximations, similar expression is also derived in Part I with the term of boundary integration in absence. We emphasize that Equation (38) is derived in an exact way. While the real displacement gradient $u_{k,\ell}(\mathbf{x})$ is unknown, we may approximate it by a *a posteriori* estimate of the coarse scale computation. Here we choose the popular Zienkiewicz–Zhu *a posteriori* estimator, i.e.

$$\bar{u}_{(k,\ell)}(\mathbf{x}) - u_{(k,\ell)}(\mathbf{x}) \approx \bar{u}_{(k,\ell)}(\mathbf{x}) - u_{(k,\ell)}^Z(\mathbf{x}) \tag{39}$$

In the above equation, $u_{(k,\ell)}^Z$ is the Zienkiewicz–Zhu recovery displacement gradient field, which will be discussed later. The difference between the Z–Z recovery field and the coarse scale field may be viewed as the residual due to discretization. Borrowing the terminology from *Micromechanics*, (e.g. Reference [5]), we refer such residual strain as *the eigenstrain*, i.e.

$$\varepsilon_{k\ell}^*(\mathbf{x}) := u_{(k,\ell)}^Z(\mathbf{x}) - \bar{u}_{(k,\ell)}(\mathbf{x}) \tag{40}$$

Hence,

$$u'_i(\mathbf{y}) = - \int_{\Omega_e^c} C_{mnkl} G_{im,n}^\infty(\mathbf{y} - \mathbf{x}) \varepsilon_{k\ell}^*(\mathbf{x}) d\Omega_x + \int_{\partial\Omega_e^c} \sigma_{kl}^{G_i^\infty}(\mathbf{y} - \mathbf{x}) n_\ell(\mathbf{x}) u'_k(\mathbf{x}) dS_x \tag{41}$$

Equation (41) is identical to the statement of an inclusion embedded in a finite domain under prescribed Neumann boundary condition, as Equation (6) in Section 2. Heuristically, we take the finite Neumann–Eshelby tensors $\mathbb{S}_{ijkl}^{I,F}$ and $\mathbb{S}_{ijkl}^{E,F}$ for a circular inclusion in a circular RVE, and rewrite the fine scale solution in a compact form as

$$\varepsilon'_{ij}(\mathbf{y}) = \mathbb{S}_{ijkl}^{I,F}(\mathbf{y}) \varepsilon_{k\ell}^*(\mathbf{y}) + \sum_{\mathbf{x} \notin \Omega_e} \mathbb{S}_{ijkl}^{E,F}(\mathbf{y} - \mathbf{x}) \varepsilon_{k\ell}^*(\mathbf{x}) \quad \text{for } \mathbf{y} \in \Omega_e \tag{42}$$

The above formulation separates the contribution to the fine scale strain into two parts: the interior part and the exterior parts. Examining the expressions of the finite Neumann–Eshelby tensors, we find $S_{ijkl}^{E,F}$ is of order $\mathcal{O}(\rho_0^2)$ and $\rho_0 < 1$ for $\mathbf{y} \notin \Omega_e^c$. This clearly shows that the exterior contribution is of second order which is much smaller than the interior contribution and decays fast when \mathbf{y} is away from Ω_e^c . Based on this fact, we make a further approximation by neglecting the exterior parts of the fine scale strain, which represents the interaction of discretization error among different elements.

That leads to the expression:

$$\varepsilon'_{ij}(\mathbf{y}) = S_{ijkl}^{I,F}(\mathbf{y}) \varepsilon_{kl}^*(\mathbf{y}) \quad \text{for } \mathbf{y} \in \Omega_e \quad (43)$$

Since no exterior Eshelby tensor is present in the fine scale solution, we simplify the notation $S_{ijkl}^{I,F}$ to S_{ijkl} without causing any confusion. A simplified fine scale solution may be expressed as follows:

$$\varepsilon'_{ij}(\mathbf{y}) = \sum_{e=1}^{n_{el}} \{S_{ijkl}(\mathbf{y})(u_{(k,\ell)}^Z(\mathbf{y}) - \bar{u}_{(k,\ell)}^c(\mathbf{y}))\chi(\Omega_e)\} \quad (44)$$

where $\chi(\Omega_e)$ is the characteristic function of the element Ω_e ,

$$\chi(\Omega_e) = \begin{cases} 1 & \mathbf{y} \in \Omega_e \\ 0 & \mathbf{y} \in \Omega_e^c/\Omega_e \end{cases} \quad (45)$$

It worths pointing out that the above formulation has exactly the same format as that in Part I, with only S_{ijkl} here representing interior Neumann–Eshelby tensor instead of infinite Eshelby tensor.

3.3. Zienkiewicz–Zhu estimate

C^0 continuity of the trial function space results in a discontinuous approximation of the coarse scale displacement gradient field across elements. More accurate displacement gradient field can be recovered from the coarse scale solution by various techniques. Following the procedure outlined in References [13, 14], the recovered displacement gradient field can be interpolated as

$$u_{(k,\ell)}^Z(\mathbf{x}) = \sum_{n=1}^{n_{ed}} N^n(\mathbf{x}) \tilde{u}_{(k,\ell)}^{Z,n} \quad (46)$$

where n_{ed} is the number of nodes in an element; $N^n(\mathbf{x})$ is the same shape function used for the interpolation of displacements; $\tilde{u}_{(k,\ell)}^{Z,n}$ is the nodal value of the displacement gradient. Superscript n is used here to denote a particular node.

It is further assumed that the nodal displacement gradient $\tilde{u}_{(k,\ell)}^{Z,n}$ belongs to a polynomial expansion of the same order as that in the shape function over the element cluster $\Omega_E^{(n)}$

surrounding the node n under consideration,

$$\tilde{u}_{(k,\ell)}^p(\mathbf{x}) = \mathbf{P}(\mathbf{x})\mathbf{a} \tag{47}$$

where \mathbf{a} is an unknown vector for the (k, ℓ) component of the strain. For a two-dimensional triangle element mesh, we may choose the polynomial basis $\mathbf{P}(\mathbf{x}) = [1, x, y]$, and for two-dimensional quadrilateral element mesh, we choose $\mathbf{P}(\mathbf{x}) = [1, x, y, xy]$.

The unknown vector \mathbf{a} is determined by minimizing the functional $E(\mathbf{a})$ defined on the element cluster $\Omega_E^{(n)}$ surrounding the node n under consideration

$$E(\mathbf{a}) = \int_{\Omega_E^{(n)}} (\tilde{u}_{(k,\ell)}^p(\mathbf{x}) - \bar{u}_{(k,\ell)}(\mathbf{x}))^2 d\Omega = \int_{\Omega_E^{(n)}} (\mathbf{P}(\mathbf{x})\mathbf{a} - \bar{u}_{(k,\ell)}(\mathbf{x}))^2 d\Omega \tag{48}$$

The minimization can be solved in matrix form as

$$\mathbf{a} = \mathbf{A}^{-1}\mathbf{b} \tag{49}$$

where

$$\mathbf{A} = \int_{\Omega_E^{(n)}} \mathbf{P}^T \mathbf{P} d\Omega \quad \text{and} \quad \mathbf{b} = \int_{\Omega_E^{(n)}} \mathbf{P}^T \bar{u}_{(k,\ell)} d\Omega \tag{50}$$

The nodal displacement gradients are then obtained by substituting appropriate co-ordinates \mathbf{x}^n of the node n into the polynomial expansion

$$\tilde{u}_{(k,\ell)}^{Z,n} = \tilde{u}_{(k,\ell)}^p(\mathbf{x}^n) = \mathbf{P}(\mathbf{x}^n)\mathbf{a} = \mathbf{P}^n \mathbf{a} \tag{51}$$

where $\mathbf{P}^n = \mathbf{P}(\mathbf{x}^n)$.

Therefore the recovered nodal displacement gradient is

$$\tilde{u}_{(k,\ell)}^{Z,n} = \mathbf{P}^n \mathbf{A}^{-1} \int_{\Omega_E^{(n)}} \mathbf{P}^T \bar{u}_{(k,\ell)} d\Omega = \int_{\Omega_E^{(n)}} \mathbf{P}^n \mathbf{A}^{-1} \mathbf{P}^T \bar{u}_{(k,\ell)} d\Omega \tag{52}$$

Note that $\mathbf{P}^n \mathbf{A}^{-1} \mathbf{P}^T$ is a scalar quantity, so the above equation states that the recovered nodal displacement gradient at a node n is a weighted average of the coarse scale displacement gradient over the element cluster $\Omega_E^{(n)}$ surrounding node n . One may also observe the non-local nature of the recovery. Zienkiewicz and Zhu [13, 14] reported superconvergence of the recovered displacement gradient field for linear elasticity problems, i.e. an $O(h^2)$ convergence for both linear triangle and bilinear quadrilateral elements. So we can approximate the exact displacement gradient in Equation (38) by the recovered field, since the latter is indeed accurate.

Substituting the above result into Equations (46) and (44), the fine scale solution over element Ω_e can be expressed analytically in terms of the coarse scale solution as

$$\varepsilon'_{ij}(\mathbf{x}) = S_{ijkl}(\mathbf{x}) \left\{ \sum_{n=1}^{ned} N^n(\mathbf{x}) \left[\int_{\Omega_E^{(n)}} \mathbf{P}^n \mathbf{A}^{-1} \mathbf{P}^T \bar{u}_{(k,\ell)} d\Omega \right] - \bar{u}_{(k,\ell)}(\mathbf{x}) \right\} \quad \forall \mathbf{x} \in \Omega_e \tag{53}$$

3.4. Modified smart element solution

With the fine scale solution obtained, the coarse scale weak formulation,

$$a(\bar{\mathbf{w}}, \bar{\mathbf{u}}) + a(\bar{\mathbf{w}}, \mathbf{u}') = (\bar{\mathbf{w}}, \mathbf{f})_{\Omega} + (\bar{\mathbf{w}}, \mathbf{t}^0)_{\Gamma_t} \quad (54)$$

can be solved. Substituting Equation (53) into Equation (54), we obtained

$$\begin{aligned} & \mathbf{A} \int_{\Omega_e} \bar{w}_{(i,j)}^e C_{ijkl} \left\{ \bar{u}_{(k,\ell)}^e + S_{klmn} \left[\sum_{n=1}^{ned} N^n(\mathbf{x}) \left(\int_{\Omega_E^{(n)}} \mathbf{P}^n \mathbf{A}^{-1} \mathbf{P}^T \bar{u}_{(m,n)}^{ej} d\Omega_x \right) - \bar{u}_{(m,n)}^e(\mathbf{x}) \right] \right\} d\Omega_x \\ &= \mathbf{A} \int_{\Omega_e} \bar{w}_i^e b_i d\Omega_x + \int_{\Gamma_t \cap \partial\Omega_e} \bar{w}_i^e t_i^0 dS_x \end{aligned} \quad (55)$$

Using finite element spatial discretization, we can write (55) in a matrix form:

$$[\mathbf{K}][\mathbf{d}] = [\mathbf{R}] \quad (56)$$

The global force vector $[\mathbf{R}]$ is the same as that in conventional finite element methods,

$$[\mathbf{R}] = \mathbf{A} \left\{ \int_{\Omega_e} [\mathbf{N}]_e^T [\mathbf{b}]_e d\Omega_x + \int_{\partial\Omega_e \cap \Gamma_t} [\mathbf{N}]_e^T [\mathbf{t}^0]_e dS_x \right\} \quad (57)$$

where the symbol \mathbf{A} is the so-called *element assembly operator* (see Reference [15]). $[\mathbf{N}]_e$ and $[\mathbf{B}]_e$ are the element shape function matrix and shape function gradient matrix, respectively. $[\mathbf{b}]_e$ is the element body force vector and $[\mathbf{t}^0]_e$ is the element traction vector.

Because of non-local nature of the Zeinkiewicz–Zhu recovery procedure, elemental DOFs in forming the stiffness matrix $[\mathbf{K}]$ are coupled through element clusters. With slightly abuse of notations, the self-adaptive stiffness matrix $[\mathbf{K}]$ can be constructed by the following nested submatrix assemblage procedure:

$$[\mathbf{K}] = \sum_{r,s \in \Omega_e} \int_{\Omega_e} [\mathbf{B}_r]^T [\mathbf{C}] \left\{ [\mathbf{B}_s] + [\mathbf{S}] \left(\sum_{t \in \Omega_E^{(s)}} [\mathbf{N}_s][\tilde{\mathbf{B}}_{st}] - [\mathbf{B}_s] \right) \right\} d\Omega_x \quad (58)$$

where r, s and t are nodal numbers in an element or in a cluster, and $[\mathbf{C}]$ and $[\mathbf{S}]$ are the matrix form of the elasticity tensor and the finite Eshelby tensor. $[\mathbf{B}_r]$ is the shape function gradient submatrix for node r . The \sum in Equation (58) should be understood as assembling the nodal submatrix (2×2 for 2D) to the corresponding global DOFs. Equation (58) represents a nested assemblage procedure: $[\tilde{\mathbf{B}}_{st}]$, the weighted nodal gradient submatrix at node s , is assembled from each node t in the element cluster $\Omega_E^{(s)}$ surrounding s . $[\tilde{\mathbf{B}}_{st}]$ is then interpolated using shape function matrix $[\mathbf{N}_s]$ of s to form the recovery solution inside Ω_e . The difference of recovery strain and coarse strain is then filtered by the finite Eshelby matrix $[\mathbf{S}]$ to form the fine scale solution. Finally, nodal DOF for nodes r, s are assembled. Algorithm 1 listed the nested assembling procedure in details. All the matrices in Equation (58) are formed explicitly for 2D plane strain formulation. Extension of these expressions to 3D formulation is obvious.

Algorithm 1. Self-adaptive stiffness matrix assemblage

1. Loop each element $\Omega_e \subset \Omega$
2. Loop each node $r \in \Omega_e$
3. Loop each node $s \in \Omega_e$
4. Assemble

$$\int_{\Omega_e} [\mathbf{B}_r]^T [\mathbf{C}] ([\mathbf{I}]-[\mathbf{S}]) [\mathbf{B}_s] d\Omega_x \rightarrow \mathbf{K}(2r-1:2r, 2s-1:2s) \tag{59}$$

5. Loop each element $e_j \subset \Omega_E^{(s)}$ (element cluster of node s)
6. Loop each node $t \in e_j$
7. Assemble

$$\int_{\Omega_e} [\mathbf{B}_r]^T [\mathbf{C}] [\mathbf{S}] [\mathbf{N}_s] [\tilde{\mathbf{B}}_{st}] d\Omega_x \rightarrow \mathbf{K}(2r-1:2r, 2t-1:2t) \tag{60}$$

where for plane strain formulation

$$[\mathbf{B}_s] = \begin{bmatrix} N_{,1}^s & 0 \\ 0 & N_{,2}^s \\ N_{,2}^s & N_{,1}^s \end{bmatrix}, \quad [\mathbf{N}_s] = \begin{bmatrix} N^s & 0 & 0 \\ 0 & N^s & 0 \\ 0 & 0 & N^s \end{bmatrix}, \quad [\mathbf{I}] = \begin{bmatrix} 1 & 0 & 0 \\ 0 & 1 & 0 \\ 0 & 0 & 1 \end{bmatrix}$$

N^s is shape function for node s .

$$[\tilde{\mathbf{B}}_{st}] = \int_{\Omega_E^{(s)}} \begin{bmatrix} \omega_s & 0 & 0 \\ 0 & \omega_s & 0 \\ 0 & 0 & \omega_s \end{bmatrix} [\mathbf{B}_t] d\Omega, \quad \omega_s = \mathbf{P}(\mathbf{x}^s) \left[\int_{\Omega_E^{(s)}} \mathbf{P}^T \mathbf{P} d\Omega \right]^{-1} \mathbf{P}^T$$

$\mathbf{P} = [1, x, y]$ for triangle element, $\mathbf{P} = [1, x, y, xy]$ for quadrilateral element.

$$[\mathbf{C}] = \begin{bmatrix} \lambda + 2G & \lambda & 0 \\ \lambda & \lambda + 2G & 0 \\ 0 & 0 & G \end{bmatrix}, \quad \lambda = \frac{\nu E}{(1+\nu)(1-2\nu)}, \quad G = \frac{E}{2(1+\nu)}$$

$$[\mathbf{S}] = \frac{1}{2} \begin{bmatrix} s_1^F + s_2^F & s_1^F - s_2^F & 0 \\ s_1^F - s_2^F & s_1^F + s_2^F & 0 \\ 0 & 0 & s_2^F \end{bmatrix}; \quad s_1^F, s_2^F \text{ refer to Equation(15).}$$

8. End loop 6.
 9. End loop 5.
 10. End loop 3.
 11. End loop 2.
 12. End loop 1.
-

4. MODAL ANALYSIS OF THE MODIFIED SMART ELEMENT

In this section, we perform a modal analysis of the modified smart element to examine its intrinsic property to avoid volumetric locking at the incompressible limit. For the sake of simplicity, we choose a single square element, and the result will be compared to that of the standard four-node quadrilateral ($Q1$) element.

Following the procedures listed in References [16, 17], the eigenvalues and eigenvectors of the element stiffness matrix are computed for the standard $Q1$ element and the modified smart element, respectively. Please note that in the single element case, the element cluster at each node only includes the featured element itself. There will still be homogenization effect. This can be seen from Equation (58): in this case, the element cluster, $\Omega_E^{(s)}$, only contains one element, nonetheless, the overall stiffness matrix is modified. Both of the stiffness matrices of the $Q1$ and the modified smart element are 8×8 for a quadrilateral setting. The eight eigenvectors of the stiffness matrices correspond to eight modes—three rigid body modes (Figure 4) for translations and rotation, three constant strain modes for the volumetric, stretch and shear modes (Figure 5), and two hourglass modes (Figure 6) representing element bending.

To study the locking effect, the eigenvalues are plotted against different Poisson's ratio ν . As shown in Figure 7, the eigenvalues of $Q1$ element and modified smart element matrices appear to be very similar for the constant strain modes. Specifically, the eigenvalues associated with the stretch mode and the shear mode stay finite as $\nu \rightarrow 0.5$, so no volumetric locking will occur for this two modes. On the other hand, the eigenvalues associated with the

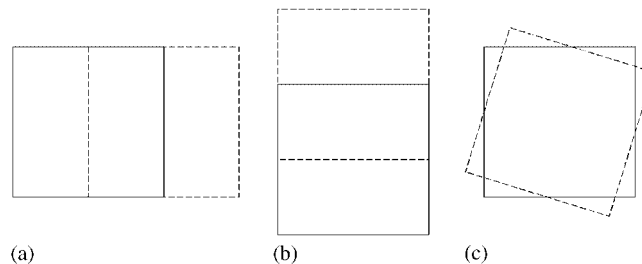


Figure 4. Rigid body modes: (a) x -direction translation; (b) y -direction translation; and (c) rotation.

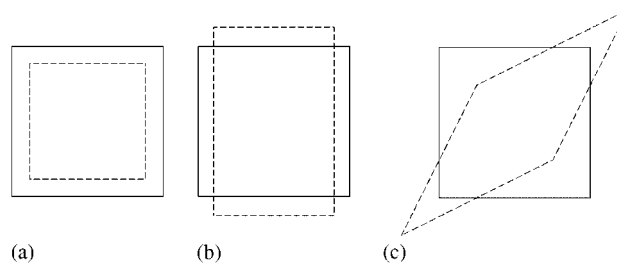


Figure 5. Constant strain modes: (a) volumetric; (b) stretch; and (c) shear.

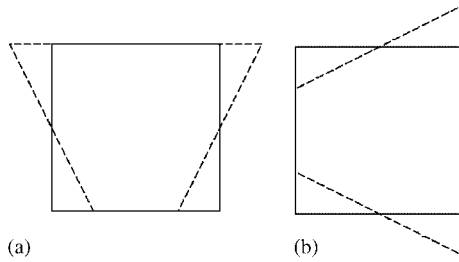


Figure 6. Hourglass modes: (a) bending I; and (b) bending II.

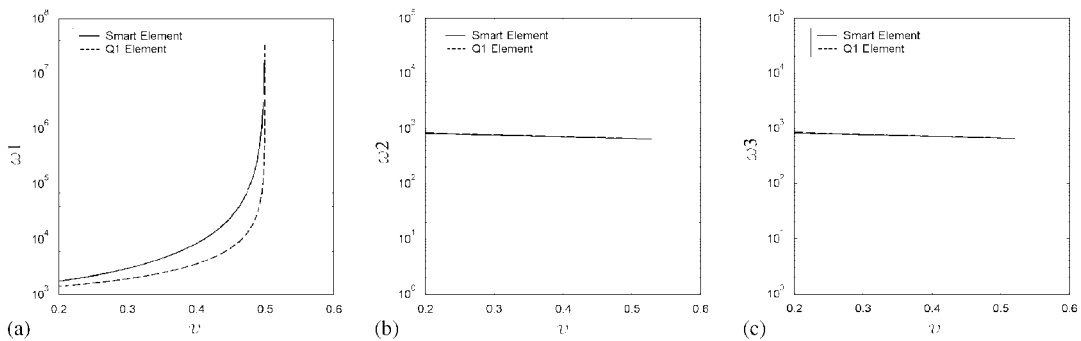


Figure 7. Comparison of constant strain eigenvalues: (a) volumetric mode; (b) stretch mode; and (c) shear mode.

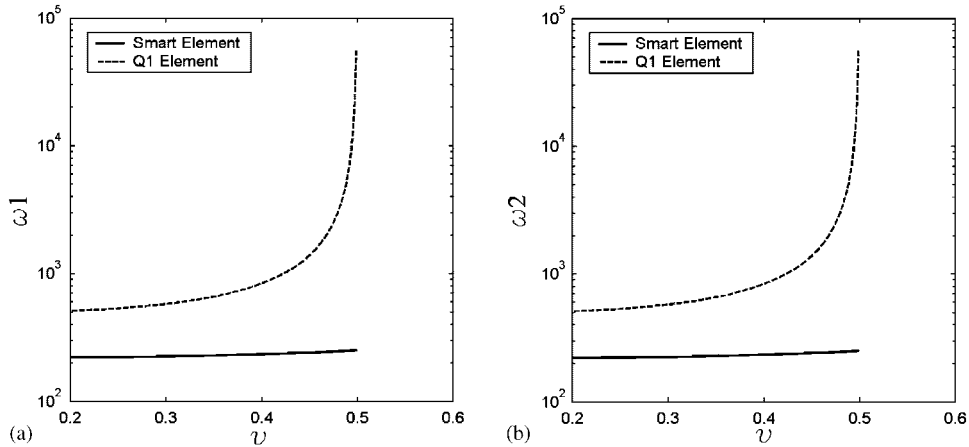


Figure 8. Comparison of the hourglass eigenvalues: (a) bending I; (b) bending II.

volumetric mode both go to infinity as $\nu \rightarrow 0.5$, which means at the incompressible limit, an infinitely large force is needed to induce the displacements of this mode. This phenomenon is *expected* for the volumetric mode to preserve volume at the incompressible limit and is

referred as *physical locking*. So no volumetric locking occurs in the constant strain modes for both elements.

Shown in Figure 8 are the eigenvalues of the two hourglass modes against ν . When $\nu \rightarrow 0.5$, the hourglass eigenvalues of $Q1$ element tend to infinity, which is referred as *non-physical locking* and is the reason for its volumetric locking phenomenon at the incompressible limit. On the other hand, the hourglass eigenvalues of smart element stay finite as $\nu \rightarrow 0.5$. So with the smart element approximation, bending can occur at the incompressible limit, i.e. the modified smart element is free of volumetric locking.

5. NUMERICAL EXAMPLES

To demonstrate the improved performance of the modified smart element, three numerical examples have been carried out by using the modified formulation: the cantilever beam problem, the problem of a plate with a hole, and the L-shaped plate problem. Numerical solutions from the conventional FEM method, the original smart element and the modified smart element method are compared in each example.

To quantify the accuracy of the numerical solutions and the rate of convergence, we used the error L_2 norm as defined in Reference [18],

$$\eta_{L_2} = \frac{\|\mathbf{e}\|_{L_2}}{\|\mathbf{u}\|_{L_2}} \quad (61)$$

where

$$\|\mathbf{e}\|_{L_2} = \left[\int_{\Omega} (\mathbf{u} - \mathbf{u}^h)^T (\mathbf{u} - \mathbf{u}^h) d\Omega \right]^{1/2} \quad (62)$$

$$\|\mathbf{u}\|_{L_2} = \left[\int_{\Omega} \mathbf{u}^T \mathbf{u} d\Omega \right]^{1/2} \quad (63)$$

with \mathbf{u} the exact solution and \mathbf{u}^h the numerical solution.

5.1. Cantilever beam

The exact solution for the bending problem of a cantilever beam subjected to end loading (Figure 9) is given by Timoshenko and Goodier [19],

$$u_x = -\frac{Py}{6\bar{E}I} \left(y - \frac{D}{2} \right) [3x(2L - x) + (2 + \bar{\nu})y(y - D)] \quad (64)$$

$$u_y = \frac{P}{6\bar{E}I} \left[x^2(3L - x) + 3\bar{\nu}(L - x) \left(y - \frac{D}{2} \right)^2 + \frac{4 + 5\bar{\nu}}{4} D^2 x \right] \quad (65)$$

where

$$I = \frac{D^3}{12} \quad (66)$$

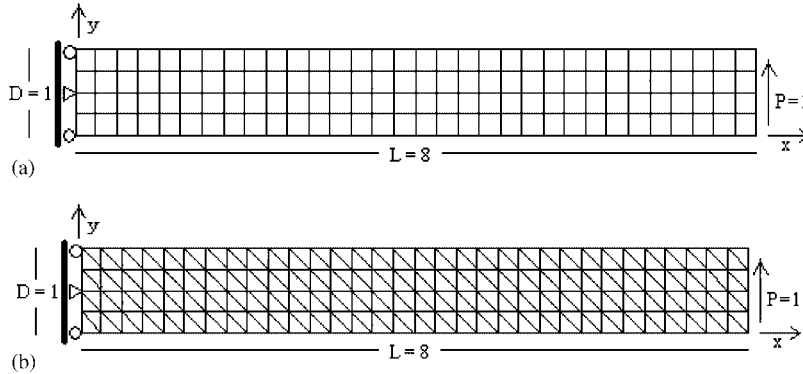


Figure 9. A cantilever beam with: (a) quadrilateral mesh; and (b) triangle mesh.

$$\bar{E} = \begin{cases} E & \text{for plane stress} \\ E/(1 - \nu^2) & \text{for plane strain} \end{cases} \tag{67}$$

$$\bar{\nu} = \begin{cases} \nu & \text{for plane stress} \\ \nu/(1 - \nu) & \text{for plane strain} \end{cases} \tag{68}$$

The corresponding stress field is

$$\sigma_{xx}(x, y) = -\frac{P}{I}(L - x) \left(y - \frac{D}{2} \right) \tag{69}$$

$$\sigma_{yy}(x, y) = 0 \tag{70}$$

$$\sigma_{xy}(x, y) = \frac{Py}{2I}(y - D) \tag{71}$$

The problem has been solved at the nearly-incompressible limit for plane strain case, with Young’s modulus $E = 1000$, Poisson’s ratio $\nu = 0.499$, and zero body force, i.e. $b_m = 0.0$. The dimensions of the beam are: $L = 8.0$ and $D = 1.0$. Figure 9 shows examples of structured quadrilateral and triangular meshes used in the analysis. In the computation, exact displacement solution is prescribed on $x = 0$ beam edge, while exact traction solution is applied along the edge $x = L$. The rest of the boundary is traction free.

The numerical results obtained via modified smart element method are compared to the exact solution, the conventional finite element solution and original smart element solution in Figure 10. At the incompressible limit, conventional FEM solution locks as expected. While both smart elements show point-wise improvement, and the modified formulation has improved accuracy over the original scheme. In term of the overall error L_2 norm, Figures 10(c) and (d) show that the convergence rate of the modified smart element is faster than the original

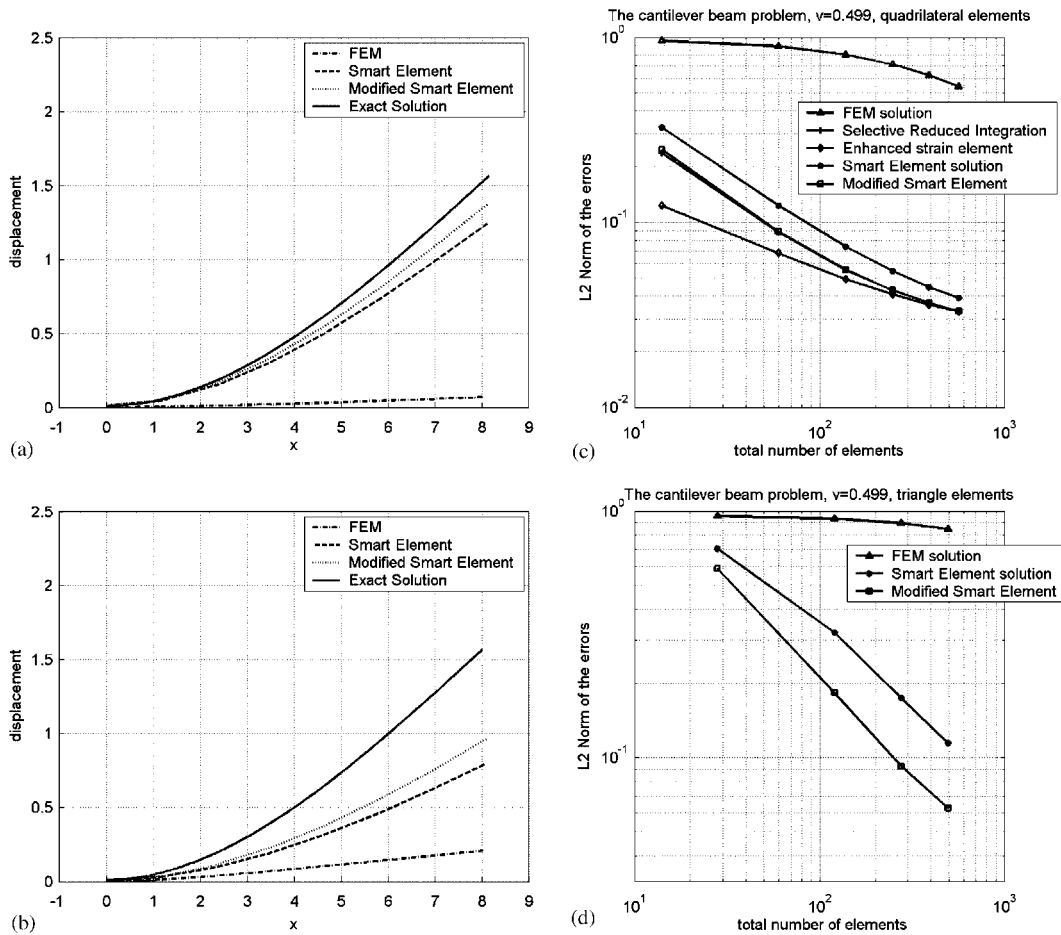


Figure 10. Comparison of modified smart element results to conventional FEM solution, smart element solution and the exact solution: (a) vertical displacement along centre line $y=0$, quadrilateral element mesh; (b) vertical displacement along centre line $y=0$, triangle element mesh; (c) log-log convergence plot in term of the L_2 norm of the error, quadrilateral element; and (d) log-log convergence plot in term of the L_2 norm of the error, triangle element.

formulation, and the rate of convergence is comparable with the selective reduced integration scheme.

For this problem, we have compared the computational cost of the proposed method with the enhanced strain method [20], which has been proven to handle incompressibility well. Both codes are written in MATLAB and run in a PC with a Pentium-III processor. The results are summarized in Table I. We can see the proposed method is computationally more expensive than the enhanced strain method.

Table I. Comparison of computational cost, with quadrilateral elements.

Method	CPU time (s) (14 elements)	CPU time (s) (60 elements)
Smart element	1.3180	7.9070
Enhanced strain	0.3810	2.4030

5.2. A plate with a hole

A finite square plate with a hole at the centre is subjected to a unit uniaxial tension along x -direction. The exact displacement solution is given as

$$u_1(r, \theta) = \frac{a}{8\mu} \left[\frac{r}{a}(\kappa + 1) \cos \theta + 2\frac{a}{r}((1 + \kappa) \cos \theta + \cos 3\theta) - 2\frac{a^3}{r^3} \cos 3\theta \right] \quad (72)$$

$$u_2(r, \theta) = \frac{a}{8\mu} \left[\frac{r}{a}(\kappa - 3) \sin \theta + 2\frac{a}{r}((1 - \kappa) \sin \theta + \sin 3\theta) - 2\frac{a^3}{r^3} \sin 3\theta \right] \quad (73)$$

where μ is the shear modulus and κ (the Kolosov constant) is defined as

$$\kappa = \begin{cases} 3 - 4\nu & \text{for plane strain} \\ \frac{3 - \nu}{1 + \nu} & \text{for plane stress} \end{cases} \quad (74)$$

The corresponding stress field is

$$\sigma_{11}(r, \theta) = 1 - \frac{a^2}{r^2} \left(\frac{3}{2} \cos 2\theta + \cos 4\theta \right) + \frac{3}{2} \frac{a^4}{r^4} \cos 4\theta \quad (75)$$

$$\sigma_{22}(r, \theta) = -\frac{a^2}{r^2} \left(\frac{1}{2} \cos 2\theta - \cos 4\theta \right) - \frac{3}{2} \frac{a^4}{r^4} \cos 4\theta \quad (76)$$

$$\sigma_{12}(r, \theta) = -\frac{a^2}{r^2} \left(\frac{1}{2} \sin 2\theta + \sin 4\theta \right) + \frac{3}{2} \frac{a^4}{r^4} \sin 4\theta \quad (77)$$

We solve the problem for the plane strain case with Young's modulus $E = 1$, Poisson's ratio $\nu = 0.499$, and zero body force, i.e. $b_m = 0.0$. Due to symmetry only one quadrant of the plate is considered for the analysis. The dimensions of one quarter of the plate and prescribed traction/displacement boundary conditions are illustrated in Figure 11(a). Note that the traction boundary condition is imposed along $x = (a + D)$ and $y = (a + D)$ by using the exact solution (75)–(77). The rest of the boundary is traction free. Figures 11(b) and (c) show two sample meshes used in computations.

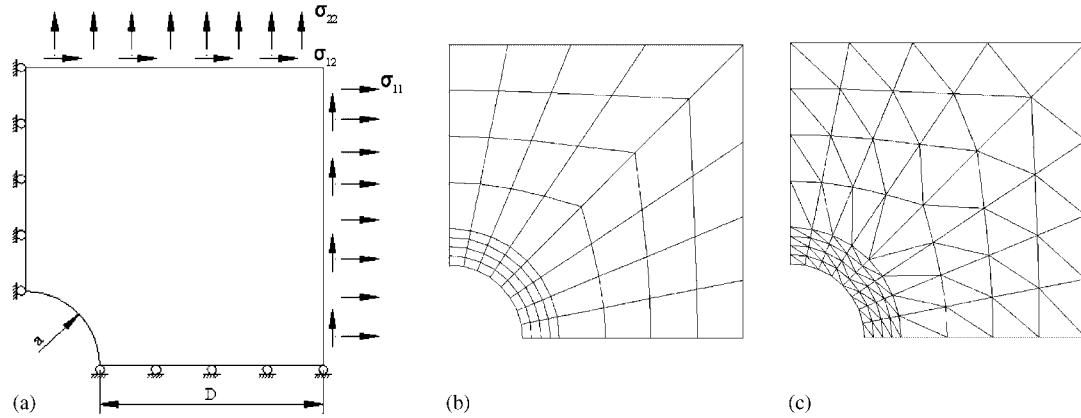


Figure 11. A plate with a hole: (a) model dimension and boundary conditions; (b) and (c) mesh examples.

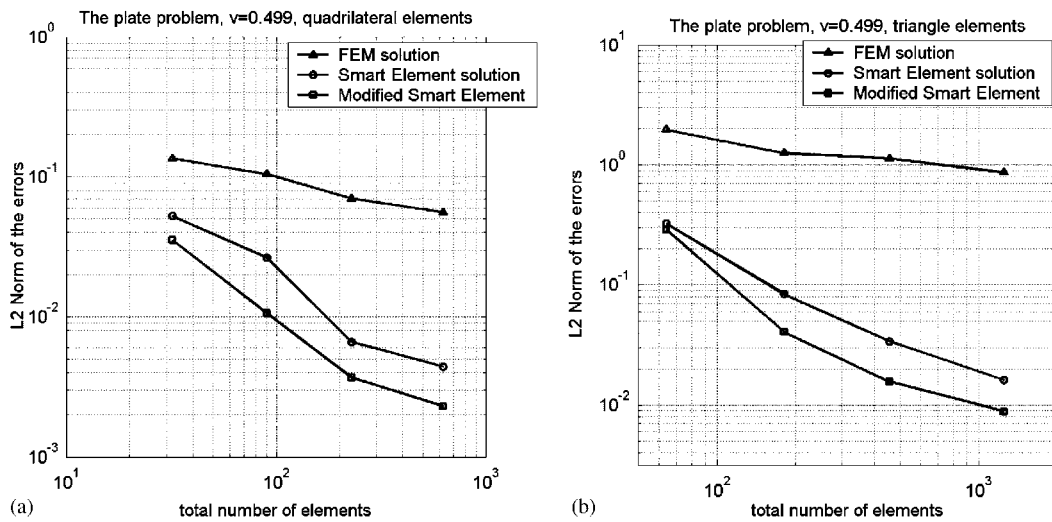


Figure 12. Convergence plots for the plate with a hole problem: (a) quadrilateral element; and (b) triangle element.

We use the smart element formulation to solve the problem under the nearly incompressible condition ($\nu \rightarrow 0.5$). It is well-known that the incompressibility will lead to volumetric locking in conventional FEM solution. We are interested in examining the performance of the smart element method under such condition, and carried out the calculations using $\nu = 0.499$.

Figures 12(a) and (b) show the convergence results. The volumetric locking in conventional FEM solution is clearly evident. The smart element solution, however, seems to be relatively unaffected by the incompressibility restriction, as the results show good overall convergence rate.

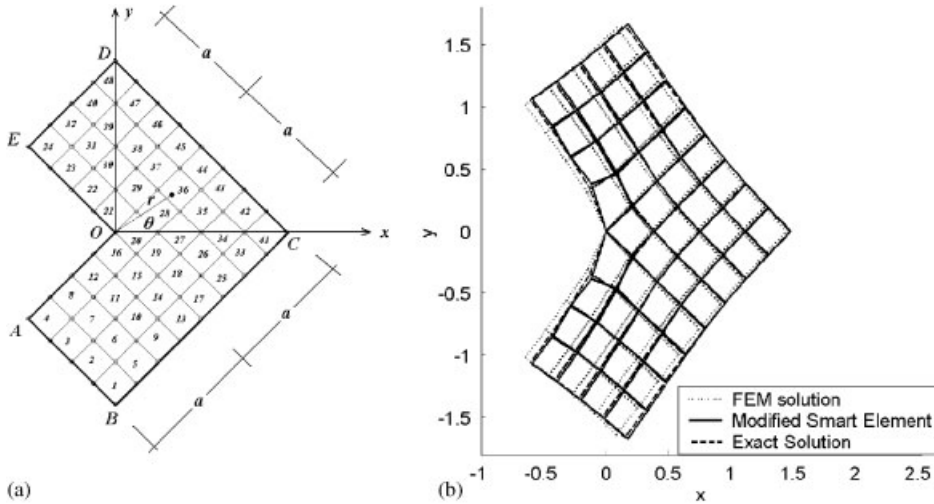


Figure 13. An L-shaped plate: (a) quadrilateral mesh; and (b) deformed meshes.

5.3. L-shaped plate

The stress field in an L-shaped plane-elastic body loaded by mode I symmetric loading is singular in the corner (e.g. Reference [21]). Convergence study of this example via p- and h-refinement of conventional finite element has been presented in Reference [22]. Here we will compare the performances of bilinear quadrilateral element and smart elements.

As shown in Figure 13(a), traction is prescribed along the exterior edges A-B-C-D-E of the plate according to the following exact stress solution:

$$\sigma_x = A_1 \lambda_1 r^{\lambda_1 - 1} [(2 - Q_1(\lambda_1 + 1)) \cos(\lambda_1 - 1)\theta - (\lambda_1 - 1) \cos(\lambda_1 - 3)\theta] \tag{78}$$

$$\sigma_y = A_1 \lambda_1 r^{\lambda_1 - 1} [(2 + Q_1(\lambda_1 + 1)) \cos(\lambda_1 - 1)\theta + (\lambda_1 - 1) \cos(\lambda_1 - 3)\theta] \tag{79}$$

$$\tau_{xy} = A_1 \lambda_1 r^{\lambda_1 - 1} [(\lambda_1 - 1) \sin(\lambda_1 - 3)\theta + Q_1(\lambda_1 + 1) \sin(\lambda_1 - 1)\theta] \tag{80}$$

where A_1 is a generalized stress-intensity factor (an arbitrary number), $\lambda_1 = 0.544483737$, $Q_1 = 0.543075579$. r and θ serve as polar co-ordinates. It is obvious that stresses are singular as $r \rightarrow 0$.

Exact solution of corresponding displacement field is known as

$$u_x = \frac{A_1}{2\mu} r^{\lambda_1} [(\kappa - Q_1(\lambda_1 + 1)) \cos \lambda\theta - \lambda_1 \cos(\lambda_1 - 2)\theta] \tag{81}$$

$$u_y = \frac{A_1}{2\mu} r^{\lambda_1} [(\kappa + Q_1(\lambda_1 + 1)) \sin \lambda\theta + \lambda_1 \sin(\lambda_1 - 2)\theta] \tag{82}$$

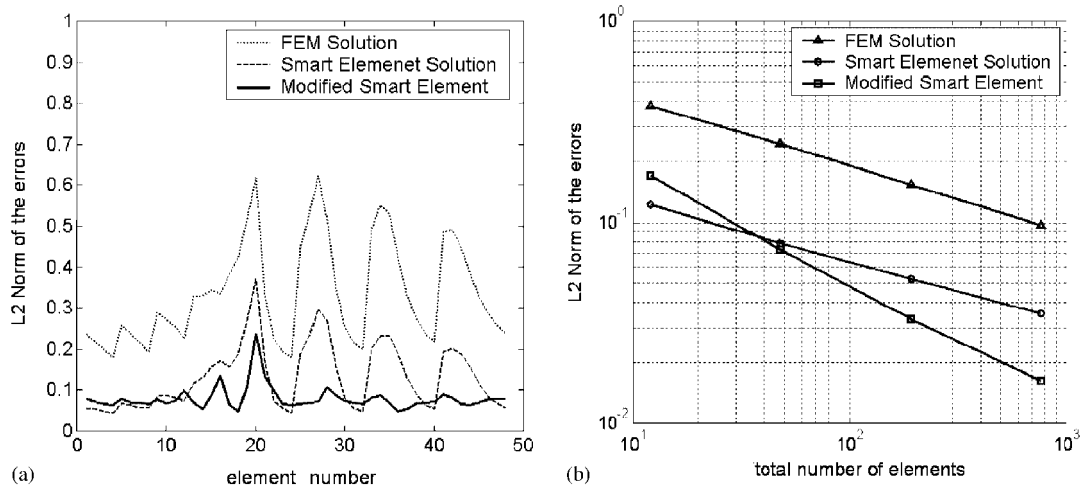


Figure 14. L-shaped plate: (a) element-wise comparison of L_2 norm of the error; and (b) log-log convergence plot in terms of the L_2 norm of the error.

where $\mu = E/2(1 + \nu)$ is the shear modulus, $\kappa = 3 - 4\nu$, ν is Poisson's ratio. We choose $\nu = 0.3$, $A_1 = 1$, $a = 1$, $E = 10$ is the example.

Figure 13(b) shows the deformed meshes computed by conventional finite element and modified smart element against the exact displacement field. Element-wise L_2 error distributions are compared among conventional finite element, original smart element, and modified smart element in Figure 14(a), where element numbers are illustrated in Figure 13(a). One may find that there is obvious improvement in element-wise errors, if the smart element is used. In particular, the modified solution tends to smooth the error distribution further with fine scale boundary condition properly integrated. Uniformly refining the mesh, convergence rates for all these methods are shown in Figure 14(b). Again, modified smart element shows improved rate of convergence.

It is worth noticing the deformed mesh of modified smart element is slightly zigzagged along edge O-A in Figure 13(b). This might arise from the fact that the fine scale is under-integrated using 2×2 Gaussian integration. While not directly addressed here, it appears that special treatment may be needed for elements at the solid boundary.

6. CONCLUDING REMARKS

In this work, the variational eigenstrain multiscale formulation is revised to incorporate fine scale contribution on the element boundary. By combining Hughes' variational multiscale decomposition, the Neumann-Eshelby tensor for a finite domain, and a simple posteriori error estimator, a self-adaptive feedback mechanism is proposed to control the errors in a Galerkin weak formulation. The resulting element formulation produced a significant improvement in the accuracy of a coarse scale numerical solution. The modified smart element shows consistent improvement over the original smart element formulation as well as conventional finite element

methods for all the numerical examples performed. Particularly, the numerical pathologies existing in traditional finite element methods, such as volumetric locking, have been overcome by using smart elements. This superior property is explained by the modal analysis.

The smart elements reported in this paper and in Part I of this work are only formulated for linear elasticity problems. Recently, Liu and Li [23] has successfully extended the method to the Stokes flow problem. We believe that the method presented here can also be extended to solve elasto-plastic problems by applying the procedures to the rate formulation, or each linearized incremental step of an updated Lagrangian formulation.

APPENDIX A: DERIVATION OF NEUMANN–ESHELBY TENSOR

In this appendix, we find the fine scale displacement field \mathbf{u}' by solving the following Fredholm type integral equation:

$$u'_m(\mathbf{y}) = \oint_{\partial\Omega} \mathbb{C}_{ijkl} u'_k(\mathbf{x}) G_{im,j}^\infty(\mathbf{y} - \mathbf{x}) n_\ell(\mathbf{x}) dS_x - \varepsilon_{k\ell}^* \int_{\Omega_e} \mathbb{C}_{ijkl} G_{im,j}^\infty(\mathbf{y} - \mathbf{x}) d\Omega_x \tag{A1}$$

which will eventually lead to the finding of Neumann–Eshelby tensor for the finite RVE.

Green’s function for two-dimensional elasto-static problem is

$$G_{ij}^\infty(\mathbf{y} - \mathbf{x}) = \frac{1}{8\pi\mu(1 - \nu)} \{ \ell_i \ell_j - (3 - 4\nu) \delta_{ij} \ln R \} \tag{A2}$$

where ν is Poisson’s ratio, μ is the shear modulus, and $\ell_i = (y_i - x_i)/R$, and $R = |\mathbf{y} - \mathbf{x}|$.

As depicted in Figure 1, the circular RVE has radius H_0 , with a circular inclusion of radius a in the centre. The ratio of inclusion and RVE is characterized by the dimensionless parameter $\rho_0 = a/H_0$. The normalized radial position for an arbitrary vector $\mathbf{y} \in \Omega_e^c$ is denoted as $t = |\mathbf{y}|/H_0$, and its circumference variation is characterized by a unit normal vector \mathbf{r} defined as $\mathbf{r}(\mathbf{y}) =: \mathbf{y}/|\mathbf{y}|$. For clarity, we reserve the symbol $\mathbf{n}(\mathbf{x}) =: \mathbf{x}/|\mathbf{x}|$ if $\mathbf{x} \in \partial\Omega_e^c$ to emphasis its position on the RVE boundary. The argument \mathbf{x} or \mathbf{y} may be dropped in the following if no confusion would occur.

A new third-order tensor, $\mathbb{U}_{imn}^{\bullet,F}(\mathbf{x})$, is introduced to characterize the disturbance displacement field in terms of the prescribed eigenstrain

$$u'_i(\mathbf{y}) = \begin{cases} \mathbb{U}_{imn}^{I,F}(\mathbf{y}) \varepsilon_{mn}^* & \forall \mathbf{y} \in \Omega_e \\ \mathbb{U}_{imn}^{E,F}(\mathbf{y}) \varepsilon_{mn}^* & \forall \mathbf{y} \in \Omega_e^c/\Omega_e \end{cases} \tag{A3}$$

such that the expected strain field solution can be obtained via differentiation,

$$\begin{aligned} \varepsilon'_{ij}(\mathbf{y}) &= \frac{1}{2}(u'_{i,j}(\mathbf{y}) + u'_{j,i}(\mathbf{y})) \\ &= \begin{cases} \frac{1}{2}(\mathbb{U}_{imn,j}^{I,F}(\mathbf{y}) + \mathbb{U}_{jmn,i}^{I,F}(\mathbf{y})) \varepsilon_{mn}^* = \mathbb{S}_{ijmn}^{I,F}(\mathbf{y}) \varepsilon_{mn}^* & \forall \mathbf{y} \in \Omega_e \\ \frac{1}{2}(\mathbb{U}_{imn,j}^{E,F}(\mathbf{y}) + \mathbb{U}_{jmn,i}^{E,F}(\mathbf{y})) \varepsilon_{mn}^* = \mathbb{S}_{ijmn}^{E,F}(\mathbf{y}) \varepsilon_{mn}^* & \forall \mathbf{y} \in \Omega_e^c/\Omega_e \end{cases} \end{aligned} \tag{A4}$$

Based on the observation that the Eshelby tensors for a circular inclusion in a circular RVE are ‘radial isotropic fourth-order tensors’, i.e. they can be decomposed into a radial basis

and a circumference basis. Using the matrix product of two one-dimensional (1D) arrays, we may express the components of the fourth-order interior and exterior Eshelby tensors in the following compact form:

$$\mathbb{S}_{ijmn}^{I,F}(\mathbf{y}) = \Theta_{ijmn}^T(\mathbf{r})\mathbf{S}^{I,F}(t) \tag{A5}$$

$$\mathbb{S}_{ijmn}^{E,F}(\mathbf{y}) = \Theta_{ijmn}^T(\mathbf{r})\mathbf{S}^{E,F}(t) \tag{A6}$$

where the 1D coefficient arrays, $\mathbf{S}^{I,F}(t)$, $\mathbf{S}^{E,F}(t)$, and the circumference basis $\Theta_{ijmn}(\mathbf{r})$ are specified as

$$\mathbf{S}^{I,F}(t) = \begin{bmatrix} S_1^{I,F}(t) \\ S_2^{I,F}(t) \\ S_3^{I,F}(t) \\ S_4^{I,F}(t) \\ S_5^{I,F}(t) \end{bmatrix}, \quad \mathbf{S}^{E,F}(t) = \begin{bmatrix} S_1^{E,F}(t) \\ S_2^{E,F}(t) \\ S_3^{E,F}(t) \\ S_4^{E,F}(t) \\ S_5^{E,F}(t) \end{bmatrix}, \quad \Theta_{ijmn}(\mathbf{r}) := \begin{bmatrix} \delta_{ij}\delta_{mn} \\ \delta_{im}\delta_{jn} + \delta_{in}\delta_{jm} \\ \delta_{ij}r_m r_n \\ r_i r_j \delta_{mn} \\ r_i r_j r_m r_n \end{bmatrix} \tag{A7}$$

Similarly, the tensor $\mathbb{U}_{imn}^{\bullet,F}(\mathbf{x})$ is a ‘third-order radial isotropic tensor’, and it can only admit the following form, which may be represented by the inner product of two 1D arrays,

$$\mathbb{U}_{imn}^{I,F}(\mathbf{x}) = \Xi_{imn}^T(\mathbf{r})\mathbf{U}^{I,F}(t) \quad \forall \mathbf{x} \in \Omega_e \tag{A8}$$

$$\mathbb{U}_{imn}^{E,F}(\mathbf{x}) = \Xi_{imn}^T(\mathbf{r})\mathbf{U}^{E,F}(t) \quad \forall \mathbf{x} \in \Omega_e^c/\Omega_e \tag{A9}$$

where the 1D arrays are defined as

$$\mathbf{U}^{I,F}(t) = \begin{bmatrix} U_1^{I,F}(t) \\ U_2^{I,F}(t) \\ U_3^{I,F}(t) \end{bmatrix}, \quad \mathbf{U}^{E,F}(t) = \begin{bmatrix} U_1^{E,F}(t) \\ U_2^{E,F}(t) \\ U_3^{E,F}(t) \end{bmatrix} \quad \text{and} \quad \Xi_{imn}(\mathbf{r}) = \begin{bmatrix} r_i \delta_{mn} \\ r_m \delta_{in} + r_n \delta_{im} \\ r_i r_m r_n \end{bmatrix} \tag{A10}$$

So the disturbance displacement field decomposes into a radial and circumference basis:

$$u'_i(\mathbf{y}) = u'_i(t, \mathbf{r}) = \varepsilon_{imn}^* \Xi_{imn}^T(\mathbf{r})\mathbf{U}^{I,F}(t) \quad \forall \mathbf{y} \in \Omega_e \tag{A11}$$

$$u'_i(\mathbf{y}) = u'_i(t, \mathbf{r}) = \varepsilon_{imn}^* \Xi_{imn}^T(\mathbf{r})\mathbf{U}^{E,F}(t) \quad \forall \mathbf{y} \in \Omega_e^c/\Omega_e \tag{A12}$$

Further, kinematic relation (A4) yields the following differential mapping that uniquely determines the radial basis for the strain and the displacement fields via

$$\mathbf{S}^{I,F}(t) = \mathfrak{D}(t)\mathbf{U}^{I,F}(t) \quad \text{and} \quad \mathbf{S}^{E,F}(t) = \mathfrak{D}(t)\mathbf{U}^{E,F}(t) \tag{A13}$$

where $\mathfrak{D}(t)$ is a differential operator defined in matrix form as

$$\mathfrak{D}(t) = \frac{1}{H_0} \begin{bmatrix} \frac{1}{t} & \frac{1}{t} - \frac{d}{dt} & -\frac{1}{t} \\ 0 & \frac{1}{2} \left(\frac{1}{t} + \frac{d}{dt} \right) & \frac{1}{2t} \\ 0 & -\frac{1}{t} + \frac{d}{dt} & \frac{2}{t} \\ -\frac{1}{t} + \frac{d}{dt} & -\frac{1}{t} + \frac{d}{dt} & \frac{1}{t} \\ 0 & 0 & -\frac{3}{t} + \frac{d}{dt} \end{bmatrix}^{3 \times 5} \tag{A14}$$

To solve the Fredholm integral equation (A1) in the form of (A11) and (A12), we substitute

$$u'_k(\mathbf{y}) = \varepsilon_{mn}^* \Xi_{kmn}^T(\mathbf{n}_x) \mathbf{U}^{E,F}(1) \quad \forall \mathbf{y} \in \partial\Omega_e^c \tag{A15}$$

into (A1), which yields

$$\begin{aligned} u'_i(\mathbf{y}) = & -\varepsilon_{mn}^* \int_{\Omega_e} \mathbb{C}_{pqmn} G_{pi,q}^\infty(\mathbf{y} - \mathbf{x}) d\Omega_x \\ & + \varepsilon_{mn}^* \oint_{\partial\Omega} \mathbb{C}_{pqkl} G_{pi,q}^\infty(\mathbf{y} - \mathbf{x}) \Xi_{kmn}^T(\mathbf{n}_x) \mathbf{U}^{E,F}(1) n_\ell(\mathbf{x}) dS_x \end{aligned} \tag{A16}$$

Depending on whether \mathbf{y} is inside or outside the inclusion, the domain integral in (A16) has two different solutions. Denote the domain integral

$$\varepsilon_{mn}^* \Xi_{imn}^T(\mathbf{r}) \mathbf{U}^{I,\infty}(t) = -\varepsilon_{mn}^* \int_{\Omega_e} \mathbb{C}_{pqmn} G_{pi,q}^\infty(\mathbf{y} - \mathbf{x}) d\Omega_x \quad \forall \mathbf{y} \in \Omega_e \tag{A17}$$

$$\varepsilon_{mn}^* \Xi_{imn}^T(\mathbf{r}) \mathbf{U}^{E,\infty}(t) = -\varepsilon_{mn}^* \int_{\Omega_e} \mathbb{C}_{pqmn} G_{pi,q}^\infty(\mathbf{y} - \mathbf{x}) d\Omega_x \quad \forall \mathbf{y} \in \Omega_e^c / \Omega_e \tag{A18}$$

and the boundary integral

$$\varepsilon_{mn}^* \Xi_{imn}^T(\mathbf{r}) \mathbf{U}^B(t) = \varepsilon_{mn}^* \oint_{\partial\Omega_e^c} \mathbb{C}_{pqkl} G_{pi,q}^\infty(\mathbf{y} - \mathbf{x}) \Xi_{kmn}^T(\mathbf{n}_x) \mathbf{U}^{E,F}(1) n_\ell(\mathbf{x}) dS_x \quad \forall \mathbf{y} \in \Omega_e^c \tag{A19}$$

Substituting (A17)–(A19) into (A16) and eliminating the circumference basis, one can find the following pair of algebraic equations for the radial coefficients,

$$\mathbf{U}^{I,F}(t) = \mathbf{U}^{I,\infty}(t) + \mathbf{U}^B(t), \quad 0 \leq t \leq a/H_0 \tag{A20}$$

$$\mathbf{U}^{E,F}(t) = \mathbf{U}^{E,\infty}(t) + \mathbf{U}^B(t), \quad a/H_0 \leq t \leq 1 \tag{A21}$$

Closed form expressions for $\mathbf{U}^{I,\infty}(t)$ and $\mathbf{U}^{E,\infty}(t)$ can be obtained by directly evaluating the domain integrals (A17) and (A18). $\mathbf{U}^{I,\infty}(t)$ and $\mathbf{U}^{E,\infty}(t)$ are obtained as follows:

$$\mathbf{U}^{I,\infty}(t) = \frac{H_0}{8(1-\nu)} \begin{bmatrix} (4\nu-1)t \\ (3-4\nu)t \\ 0 \end{bmatrix}, \quad \mathbf{U}^{E,\infty}(t) = \frac{\rho_0^2 H_0}{8(1-\nu)t} \begin{bmatrix} 4\nu-2 + \frac{\rho_0^2}{t^2} \\ 2-4\nu + \frac{\rho_0^2}{t^2} \\ 4 \left(1 - \frac{\rho_0^2}{t^2}\right) \end{bmatrix} \tag{A22}$$

It is noted that, when subjected to the differential operator (A14), the Eshelby tensor for an infinite RVE is recovered. i.e.

$$\mathbf{S}^{I,\infty}(t) = \mathfrak{D}(t)\mathbf{U}^{I,\infty}(t) \quad \text{and} \quad \mathbf{S}^{E,\infty}(t) = \mathfrak{D}(t)\mathbf{U}^{E,\infty}(t) \tag{A23}$$

Boundary contribution $\mathbf{U}^B(t)$ can be evaluated directly from (A19) as

$$\varepsilon_{mn}^* \Xi_{imn}^T(\mathbf{r})\mathbf{U}^B(t) = \varepsilon_{mn}^* \oint_{\partial\Omega} \mathcal{H}_{imn}(\mathbf{x}, \mathbf{y}) dS_x \tag{A24}$$

where

$$\begin{aligned} \mathcal{H}_{imn} &= \mathbb{C}_{pqkl} G_{pi,q}^\infty(\mathbf{y}-\mathbf{x}) \Xi_{kmn}^T(\mathbf{n}_x)\mathbf{U}^{E,F}(1)n_\ell(\mathbf{x}) \\ &= \frac{1}{4\pi(1-\nu)R} \{U_1^{E,F}(1)[(1-2\nu)(2n_i n_p \ell_p \delta_{mn} - \ell_i \delta_{mn}) + 2\ell_i n_p \ell_p n_q \ell_q \delta_{mn}] \\ &\quad + U_2^{E,F}(1)[(1-2\nu)(n_m n_p \ell_p \delta_{in} + n_n n_p \ell_p \delta_{im} + n_i n_m \ell_n + n_i n_n \ell_m \\ &\quad - 2n_m n_n \ell_i) + 2n_m \ell_i \ell_n n_p \ell_p + 2n_n \ell_i \ell_m n_p \ell_p] \\ &\quad + U_3^{E,F}(1)[(1-2\nu)(2n_i n_m n_n \ell_p n_p - n_m n_n \ell_i) + 2n_m n_n \ell_i n_p \ell_p n_q \ell_q]\} \end{aligned} \tag{A25}$$

Integral (A24) can be integrated exactly. After some algebraic manipulation, the final result is expressed in compact matrix form as

$$\mathbf{U}^B(t) = \mathbf{K}(t) \mathbf{U}^{E,F}(1) \tag{A26}$$

where

$$\mathbf{K}(t) = \frac{1}{4(1-\nu)} \begin{bmatrix} 2(1-2\nu)t & (1-4\nu)t & -2\nu t + \nu t^3 \\ 0 & t & t + \frac{2\nu-3}{2}t^3 \\ 0 & 0 & (3-4\nu)t^3 \end{bmatrix} \tag{A27}$$

The term, $\mathbf{U}^B(t)$, represents the boundary correction due to a finite RVE in the disturbance displacement field. This reduces the system of Equations (A20) and (A21) to

$$\mathbf{U}^{I,F}(t) = \mathbf{U}^{I,\infty}(t) + \mathbf{K}(t)\mathbf{U}^{E,F}(1), \quad 0 \leq t \leq a/H_0 \tag{A28}$$

$$\mathbf{U}^{E,F}(t) = \mathbf{U}^{E,\infty}(t) + \mathbf{K}(t)\mathbf{U}^{E,F}(1), \quad a/H_0 \leq t < 1 \tag{A29}$$

Assume that $\mathbf{U}^{I,F}(t)$ and $\mathbf{U}^{E,F}(t)$ depend on t continuously. Let $t \rightarrow 1$. One can solve for $\mathbf{U}^{E,F}(1)$ by letting $t = 1$ in (A29), i.e.

$$\mathbf{U}^{E,F}(1) = [1 - \mathbf{K}(1)]^{-1}\mathbf{U}^{E,\infty}(1) \tag{A30}$$

which gives

$$\mathbf{U}^{E,F}(1) = H_0 \begin{bmatrix} \frac{1}{2}\rho_0^2(\rho_0^2 - 1) \\ \frac{1}{2}\rho_0^4 \\ 2\rho_0^2(1 - \rho_0^2) \end{bmatrix} \tag{A31}$$

Substituting (A31) back into (A28) and (A29), one can first find,

$$\mathbf{U}^B(t) = \frac{\rho_0^2 H_0}{8(1 - \nu)} \begin{bmatrix} (3\rho_0^2 - 4\nu - 2)t + 4\nu(1 - \rho_0^2)t^3 \\ (4 - 3\rho_0^2)t + 2(2\nu - 3)(1 - \rho_0^2)t^3 \\ 4(3 - 4\nu)(1 - \rho_0^2)t^3 \end{bmatrix} \tag{A32}$$

and subsequently one can solve for both $\mathbf{U}^{I,F}(t)$ and $\mathbf{U}^{E,F}(t)$, which are the radial basis for the interior and exterior disturbance displacement fields in a finite domain,

$$\mathbf{U}^{I,F}(t) = \frac{H_0}{8(1 - \nu)} \begin{bmatrix} (4\nu - 1)t \\ (3 - 4\nu)t \\ 0 \end{bmatrix} + \frac{\rho_0^2 H_0}{8(1 - \nu)} \begin{bmatrix} (3\rho_0^2 - 4\nu - 2)t + 4\nu(1 - \rho_0^2)t^3 \\ (4 - 3\rho_0^2)t + 2(2\nu - 3)(1 - \rho_0^2)t^3 \\ 4(3 - 4\nu)(1 - \rho_0^2)t^3 \end{bmatrix} \quad 0 \leq t \leq a/H_0 \tag{A33}$$

$$\mathbf{U}^{E,F}(t) = \frac{\rho_0^2 H_0}{8(1 - \nu)} \begin{bmatrix} \frac{4\nu - 2}{t} + \frac{\rho_0^2}{t^3} \\ \frac{2 - 4\nu}{t} + \frac{\rho_0^2}{t^3} \\ \frac{4}{t} - 4\frac{\rho_0^2}{t^3} \end{bmatrix}$$

$$+ \frac{\rho_0^2 H_0}{8(1-\nu)} \begin{bmatrix} (3\rho_0^2 - 4\nu - 2)t + 4\nu(1 - \rho_0^2)t^3 \\ (4 - 3\rho_0^2)t + 2(2\nu - 3)(1 - \rho_0^2)t^3 \\ 4(3 - 4\nu)(1 - \rho_0^2)t^3 \end{bmatrix} \quad a/H_0 \leq t \leq 1 \quad (A34)$$

The radial coefficients for the Eshelby tensor can be obtained by applying differentiation operator (A14) to Equations (A33) and (A34),

$$\mathbf{S}^{I, F}(t) = \mathfrak{D}(t)\mathbf{U}^{I, F}(t) = \frac{1}{8(1-\nu)} \begin{bmatrix} 4\nu - 1 \\ 3 - 4\nu \\ 0 \\ 0 \\ 0 \end{bmatrix} + \frac{\rho_0^2}{8(1-\nu)} \begin{bmatrix} -2(1 + 2\nu) + 3\rho_0^2 + 12(1 - \rho_0^2)\nu t^2 \\ 4 - 3\rho_0^2 - 6(1 - \rho_0^2)t^2 \\ 12(1 - 2\nu)(1 - \rho_0^2)t^2 \\ 0 \\ 0 \end{bmatrix} \quad (A35)$$

$$\mathbf{S}^{E, F}(t) = \mathfrak{D}(t)\mathbf{U}^{E, F}(t)$$

$$= \frac{\rho_0^2}{8(1-\nu)} \begin{bmatrix} \frac{-2(1 + 2\nu)}{t^2} + \frac{9\rho_0^2}{t^4} \\ \frac{2}{t^2} - \frac{3\rho_0^2}{t^4} \\ \frac{4(1 + 2\nu)}{t^2} - \frac{12\rho_0^2}{t^4} \\ \frac{4}{t^2} - \frac{12\rho_0^2}{t^4} \\ -\frac{16}{t^2} + \frac{24\rho_0^2}{t^4} \end{bmatrix} + \frac{\rho_0^2}{8(1-\nu)} \begin{bmatrix} -2(1 + 2\nu) + 3\rho_0^2 + 12(1 - \rho_0^2)\nu t^2 \\ 4 - 3\rho_0^2 - 6(1 - \rho_0^2)t^2 \\ 12(1 - 2\nu)(1 - \rho_0^2)t^2 \\ 0 \\ 0 \end{bmatrix} \quad (A36)$$

The exact expressions for the Eshelby tensors for a circular inclusion embedded in a circular RVE under prescribed traction boundary condition are given as follows:

$$\begin{aligned} \mathbb{S}_{ijmn}^{I, F}(\mathbf{y}) &= \frac{1}{8(1-\nu)} \{ [(4\nu - 1)(1 - \rho_0^2) - 3\rho_0^2(1 - \rho_0^2)(1 - 4\nu t^2)] \delta_{ij} \delta_{mn} \\ &\quad + [(3 - 4\nu) + \rho_0^2 + 3\rho_0^2(1 - \rho_0^2)(1 - 2t^2)] (\delta_{im} \delta_{jn} + \delta_{in} \delta_{jm}) \\ &\quad + [12(1 - 2\nu)\rho_0^2(1 - \rho_0^2)t^2] \delta_{ij} r_m r_n \} \quad \forall \mathbf{y} \in \Omega_e \end{aligned} \quad (A37)$$

$$\begin{aligned}
 \mathbb{S}_{ijmn}^{E,F}(\mathbf{y}) = & \frac{\rho_0^2}{8(1-\nu)} \left\{ \left[-2(1+2\nu) \left(\frac{1}{t^2} + 1 \right) + 12\nu t^2 + \rho_0^2 \left(\frac{9}{t^4} + 3 - 12\nu t^2 \right) \right] \delta_{ij} \delta_{mn} \right. \\
 & + \left[\frac{2}{t^2} + 4 - 6t^2 - 3\rho_0^2 \left(\frac{1}{t^4} + 1 - 2t^2 \right) \right] (\delta_{im} \delta_{jn} + \delta_{in} \delta_{jm}) \\
 & + \left[4 \left(\frac{1+2\nu}{t^2} + 3(1-2\nu)t^2 \right) - 12\rho_0^2 \left(\frac{1}{t^4} + (1-2\nu)t^2 \right) \right] \delta_{ij} r_m r_n \\
 & + \left[\frac{4}{t^2} \left(1 - \frac{3\rho_0^2}{t^2} \right) \right] \delta_{mn} r_i r_j \\
 & \left. + \left[\frac{8}{t^2} \left(\frac{3\rho_0^2}{t^2} - 2 \right) \right] r_i r_j r_m r_n \right\} \quad \forall \mathbf{y} \in \Omega_e^c / \Omega_e
 \end{aligned} \tag{A38}$$

Expressions (A33), (A34), (A37), and (A38) can be re-cast into a unified form,

$$\mathbf{S}^F(t) = \mathbf{S}^\infty(t) + \mathbf{S}^B(t), \quad 0 \leq t \leq 1 \tag{A39}$$

$$\mathbf{U}^F(t) = \mathbf{U}^\infty(t) + \mathbf{U}^B(t), \quad 0 \leq t \leq 1 \tag{A40}$$

We emphasize that the solution in a finite RVE is essentially composed of the infinite domain solution and the boundary correction.

The induced disturbance traction field on a set of successive concentric circular surfaces can be determined using

$$t'_i(\mathbf{y}) = \sigma'_{ji}(\mathbf{y}) r_j(\mathbf{y}) \tag{A41}$$

In view of Eshelby tensors (A37)–(A38), the disturbance traction field can be specified as

$$t'_i(\mathbf{y}) = \begin{cases} r_j(\mathbf{y}) \mathbb{C}_{ijkl} (\mathbb{S}_{klmn}^{I,F}(\mathbf{y}) - \mathbb{I}_{klmn}^{(4s)}) \varepsilon_{mn}^* & \forall \mathbf{y} \in \Omega_e \\ r_j(\mathbf{y}) \mathbb{C}_{ijkl} \mathbb{S}_{klmn}^{E,F}(\mathbf{x}) \varepsilon_{mn}^* & \forall \mathbf{y} \in \Omega_e^c / \Omega_e \end{cases} \tag{A42}$$

where $\mathbb{I}_{klmn}^{(4s)}$ is the fourth-order symmetric identity tensor. It is noted that it also falls into our new category of a *fourth-order radial isotropic tensor*.

Simple calculation reveals that $t'_i(\mathbf{y})$ can also be characterized using a third-order radial isotropic tensor $\mathbb{T}_{imn}(\mathbf{y})$, which can be further decomposed into a radial and circumference basis such that

$$t'_i(\mathbf{y}) = \begin{cases} \mathbb{T}_{imn}^{I,F}(\mathbf{r}) \varepsilon_{mn}^* = \Xi_{imn}^T(\mathbf{r}) \mathbf{T}^{I,F}(t) \varepsilon_{mn}^* & \forall \mathbf{y} \in \Omega_e \\ \mathbb{T}_{imn}^{E,F}(\mathbf{r}) \varepsilon_{mn}^* = \Xi_{imn}^T(\mathbf{n}) \mathbf{T}^{E,F}(t) \varepsilon_{mn}^* & \forall \mathbf{y} \in \Omega_e^c / \Omega_e \end{cases} \tag{A43}$$

with the radial basis being determined by

$$\mathbf{T}^{I, F}(t) = \frac{\mu}{1-2\nu} \begin{bmatrix} 2S_1^{I, F}(t) + 4\nu S_2^{I, F}(t) + 2(1-\nu)S_4^{I, F}(t) - 2\nu \\ 2(1-2\nu)S_2^{I, F}(t) - (1-2\nu) \\ 2S_3^{I, F}(t) + 2(1-\nu)S_5^{I, F}(t) \end{bmatrix} \quad 0 \leq t \leq a/H_0 \quad (\text{A44})$$

$$\mathbf{T}^{E, F}(t) = \frac{\mu}{1-2\nu} \begin{bmatrix} 2S_1^{E, F}(t) + 4\nu S_2^{E, F}(t) + 2(1-\nu)S_4^{E, F}(t) \\ 2(1-2\nu)S_2^{E, F}(t) \\ 2S_3^{E, F}(t) + 2(1-\nu)S_5^{E, F}(t) \end{bmatrix} \quad a/H_0 \leq t \leq 1 \quad (\text{A45})$$

It is readily verified that when $t = 1$,

$$\mathbf{T}^{E, F}(1) = \begin{bmatrix} 0 \\ 0 \\ 0 \end{bmatrix} \quad (\text{A46})$$

This means that the traction vector vanishes at the boundary of the RVE, i.e. $t'_i(\mathbf{y}) \equiv 0$ for $\forall \mathbf{y} \in \partial\Omega_e^c$. This verifies that the prescribed Neumann boundary condition is exactly satisfied by the Neumann–Eshelby solution obtained.

ACKNOWLEDGEMENTS

This work is supported by a NSF grant (Grant No. CMS-0239130) to Professor Shaofan Li. Gang Wang also gratefully acknowledge financial support from Pacific Earthquake Engineering Research (PEER) Center through NSF Award No. EEC-9701568.

REFERENCES

1. Li S, Liu X, Gupta A. Smart element I. The Zienkiewicz–Zhu feedback. *International Journal for Numerical Methods in Engineering* 2005; **62**:1264–1294.
2. Li S, Sauer R, Wang G. Circular inclusion in a finite elastic domain. I. The Dirichlet–Eshelby problem. *Acta Mechanica* 2005, in press.
3. Wang G, Li S, Sauer R. Circular inclusion in a finite elastic domain. II. The Neumann–Eshelby problem. *Acta Mechanica* 2005, in press.
4. Li S, Gupta A, Liu X, Mahyari M. Variational eigenstrain multiscale finite element method. *Computer Methods in Applied Mechanics and Engineering* 2004; **193**:1803–1824.
5. Mura T. *Micromechanics of Defects in Solids*. Martinus Nijhoff Publishers: Dordrecht, 1987.
6. Somigliana C. Sopra l'equilibrio di un corpo elastico isotropo. *Il Nuovo Cimento* 1886; 17–19.
7. Eshelby JD. The determination of the elastic field of an ellipsoidal inclusion and related problems. *Proceedings of the Royal Society of London* 1957; **A241**:376–396.
8. Eshelby JD. The elastic field outside an ellipsoidal inclusion. *Proceedings of the Royal Society of London* 1959; **A252**:561–569.
9. Eshelby JD. Elastic inclusions and inhomogeneities. In *Progress in Solid Mechanics*, Sneddon IN, Hill R (eds), vol. 2. North-Holland: Amsterdam, 1961; 89–140.

10. Adams RA. *Sobolev Spaces*. Academic Press: New York, San Francisco, London, 1975.
11. Brenner SC, Scott LR. *The Mathematical Theory of Finite Element Methods*. Springer: New York, 1994.
12. Hughes TJR, Feijoo GR, Mazzei L, Quincy J-B. The variational multiscale method—a paradigm for computational mechanics. *Computer Methods in Applied Mechanics and Engineering* 1998; **166**:3–24.
13. Zienkiewicz OC, Zhu JZ. The superconvergent patch recovery and *a posteriori* error estimates: Part I. The recovery technique. *International Journal for Numerical Methods in Engineering* 1992; **33**:1331–1364.
14. Zienkiewicz OC, Zhu JZ. The superconvergent patch recovery and *a posteriori* error estimates: Part II. Error estimates and adaptivity. *International Journal for Numerical Methods and Engineering* 1992; **33**: 1365–1382.
15. Hughes TJR. *The Finite Element Method*. Prentice-Hall: Englewood Cliffs, NJ, 1987.
16. Armero F. *On the Locking of Standard Finite Elements*. CE232 Classnotes, University of California, Berkeley, 2002.
17. Huerta A, Fernandez-Mendez S. Locking at the incompressible limit for the element-free Galerkin method. *International Journal for Numerical Methods in Engineering* 2001; **51**:1361–1383.
18. Zienkiewicz OC, Taylor RL. *The Finite Element Method, vol. 1. The Basis* (5th edn). Butterworth-Heinemann: Stoneham, MA, 2000.
19. Timoshenko SP, Goodier JN. *Theory of Elasticity* (3rd edn). McGraw-Hill: New York, 1970.
20. Simo JC, Rifai SM. A class of mixed assumed strain methods and the method of incompatible modes. *International Journal for Numerical Methods in Engineering* 1990; **29**:1595–1638.
21. Williams ML. Stress singularities resulting from various boundary conditions in angular corners of plates in extension. *Journal of Applied Mechanics* (ASME) 1952; **19**:526–528.
22. Szabó BA. Mesh design for the p-version of the finite element method. *Computer Methods in Applied Mechanics and Engineering* 1986; **55**:181–197.
23. Liu X, Li S. A variational multiscale stabilized FEM for the 2D Stokes problem. *Finite Elements in Analysis and Design* 2005, Submitted.